

## Functional Imaging Introduction: Gaining new insight from biophotonic imaging

Mark B. Cannell

*Department of Physiology, School of Medical Sciences,  
The University of Auckland, Auckland, New Zealand*

Over the past 2 decades, there has been an explosive growth in the range of measurement modalities available to the physiologist. Today, a very large part of the electromagnetic spectrum is used to probe and record physiological function from the level of the whole body to tissue, cell and even organelle. This use of photonic methods includes radio waves in the form of nuclear magnetic resonance imaging, through light in, for example, microscopy and video imaging, and on to real time fluoroscopy with Xrays. Even gamma rays from radioisotopes find some imaging applications with gamma ray cameras. Perhaps the most common use of photonics in physiological research is in the area of microscopy and cell biology. Here we see methods that employ almost most of the fundamental features of light itself to generate physiological images; for example polarization and interference are routinely used to help generate contrast within unlabelled cells.

The effort to clarify cell function has been aided by the development of a wide variety of probes that reveal elements of cell function that cannot be directly observed through other contrast enhancement methods. With these probes we can now image intracellular ion levels, vesicle trafficking and even protein synthesis and degradation within living cells. Although today we talk about “cell biology”, “neuroscience” and “developmental biology” as cutting edge disciplines, in reality they are simply physiological research repackaged to detach the term “physiology”. It is possible that a part of this has arisen from the view that the more classical forms of physiology involved rather more quantification, mathematics and physics than is palatable for many students. This is a pity, for careful measurement can often be more revealing than cursory examination. For example, digital imaging microscopy is routinely used in all of the above disciplines but detailed analysis of the already digitized data is rarely performed. Unfortunately, the massive amount of real data contained in microscopic images is frequently ignored and image processing applied to only “beautify” images rather than provide feature extraction and quantification. I cannot help but wonder what Bernstein and Starling would have made of this “science”.

Measurement within new imaging methods has given powerful insight in to cell function. As an example, our discovery and quantification of microscopic calcium sparks<sup>1-3</sup> has shown that signal transduction occurs in microscopic domains where behaviour cannot be deduced from whole cell measurements. Such experiments have firmly established the need for confocal microscopy in live cell imaging. Today, I am still amazed that we have been now been able to directly measure microscopic gradients of

calcium within sarcomeres with a fast confocal line scanning method<sup>4</sup>. Two decades ago, such gradients could only be deduced from computer models of my rather poor quality calcium signals obtained using aequorin<sup>5,6</sup>. That such exquisitely sensitive methods can now be routinely applied to follow cellular processes promises great insight into cell physiology. This has been aided by the co-development of better probes for cell function (as well as instrumentation).

In the area of calcium metabolism, calcium imaging inside cells is not new; for example in 1928 Pollack<sup>7</sup> injected an amoeba with alarazin which precipitated as a calcium salt at the site of pseudopod formation. With increasing awareness of the multiple roles of calcium new methods were developed to image Ca and obtain sub-cellular resolution. Autoradiographic imaging of <sup>45</sup>Ca with electron microscopy was applied to muscle in the 1960's<sup>8,9</sup>. The development of calcium measurement techniques occurred quite rapidly around 1980 (see 10 for review). To improve temporal response and the ability to directly measure function in living cells required the development and application of more sensitive compounds (e.g. aequorin and metallochromic indicators) and ultimately fluorescent probes such as fura-2<sup>11,12</sup>. The high signal strength of the fluorescent probes made real time video fluorescence imaging possible<sup>13,14</sup>. The spatial resolution of the fluorescent microscope was been improved by the development and application of laser scanning confocal microscopy<sup>15-18</sup>. Such laser scanning methods promise resolution to the level of single molecules within cells – although it is always questionable whether the study of the interactions of single molecules really falls under the umbrella of “physiology”. More uncommon microscopic imaging modalities are still developed in areas such as non-linear excitation in multiphoton microscopy, fluorescence energy transfer, quantitative birefringence and quantitative phase microscopy. These methods are bringing a new generation of physicists and engineers into the life sciences and helping to further accelerate our development and application of new methods.

That visible light has proved so useful for studying cell function is easy to explain. In order to measure something it must be probed by energy in some form and to maximize the signal to noise ratio, you need to employ the highest possible energy levels. Since the energy of the visible wavelength photon (~2 eV) is somewhat lower than that of a typical chemical bond, molecules can be repeatedly probed by visible wavelength photons without destroying them. Of course, the energy difference is not so large that damage can be ignored, but with careful experimental design we can record cell function and cell

responses to many stimuli and bracket responses with controls. In live cell imaging, noisy signals are to be expected and not to be confused with poor experimentation. Therein lies the true artistry of vital imaging: to achieve the clearest possible imaging results while treading carefully along the boundary of cell damage. In connection with this point, we should also not forget that introducing any probe carries the risk of changing cell function and that molecular biological manipulation to make the cell report its own functions is also not without the risk of changing cell function/behaviour.

In summary, I suggest that the greatest advances in understanding physiological function have come about from the development and application of new measurement methods and the physiologist has always been quick and creative in applying new methods to problems in his/her area of research. Application of these new methods is always harder than using well established methods but the rewards are also greater. Thus while imaging is not new in physiological research, new imaging modalities are giving fresh insight into cell behaviour. The application of new imaging technologies within the life sciences is likely to continue to reveal unexpected complexity in physiology and life. In the following four papers presented in this symposium, we can see examples of the latest quantitative imaging techniques. As we continue this work, we can also take a moment to enjoy the beauty of the images that can be made.

## References

- Cheng H, Lederer WJ, Cannell MB. Calcium sparks: elementary events underlying excitation-contraction coupling in heart muscle. *Science* 1993;**262**(5134):740-4.
- Cannell MB, Cheng H, Lederer WJ. Spatial non-uniformities in  $[Ca^{2+}]_i$  during excitation-contraction coupling in cardiac myocytes. *Biophys. J.* 1994;**67**(5):1942-56.
- Cannell MB, Cheng H, Lederer WJ. The control of calcium release in heart muscle. *Science* 1995;**268**(5213):1045-9.
- Hollingworth S, Soeller C, Baylor SM, Cannell MB. Sarcomeric  $Ca^{2+}$  gradients during activation of frog skeletal muscle fibres imaged with confocal and two-photon microscopy. *J. Physiol.* 2000;**526 Pt 3**:551-60.
- Cannell MB, Allen DG. Model of calcium movements during activation in the sarcomere of frog skeletal muscle. *Biophys. J.* 1984;**45**(5):913-25.
- Cannell MB. Effect of tetanus duration on the free calcium during the relaxation of frog skeletal muscle fibres. *J. Physiol.* 1986;**376**:203-18.
- Pollack H. Micrurgical studies in cell physiology. IV. Calcium ions in living protoplasm. *J. Gen. Physiol.* 1928;**11**: p. 539-545.
- Winegrad, S., Autoradiographic studies of intracellular calcium in frog skeletal muscle. *J. Gen. Physiol.* 1965;**48**:455-79.
- Winegrad, S., Intracellular calcium movements of frog skeletal muscle during recovery from tetanus. *J. Gen. Physiol.* 1968;**51**(1):65-83.
- Blinks JR, Wier WG, Hess P, Prendergast FG. Measurement of  $Ca^{2+}$  concentrations in living cells. *Prog. Biophys. Mol. Biol.* 1982;**40**(1-2):1-114.
- Grynkiewicz G, Poenie M, Tsien RY. A new generation of  $Ca^{2+}$  indicators with greatly improved fluorescence properties. *J. Biol. Chem.* 1985;**260**(6):3440-50.
- Poenie M, Tsien R. Fura-2: a powerful new tool for measuring and imaging  $[Ca^{2+}]_i$  in single cells. *Prog. Clin. Biol. Res.* 1986;**210**:53-6.
- Wier WG, Cannell MB, Berlin JR, Marban E, Lederer WJ. Cellular and subcellular heterogeneity of  $[Ca^{2+}]_i$  in single heart cells revealed by fura-2. *Science* 1987;**235**(4786):325-8.
- Cannell MB, Berlin JR, Lederer WJ. Intracellular calcium in cardiac myocytes: calcium transients measured using fluorescence imaging. *Soc. Gen. Physiol. Ser.* 1987;**42**:201-14.
- Brakenhoff GJ, van der Voort HT, van Spronsen EA, Linnemans WA, Nanninga N. Three-dimensional chromatin distribution in neuroblastoma nuclei shown by confocal scanning laser microscopy. *Nature* 1985;**317**(6039):748-9.
- White JG, Amos WB, Fordham M. An evaluation of confocal versus conventional imaging of biological structures by fluorescence light microscopy. *J. Cell Biol.* 1987;**105**(1):41-8.
- Brakenhoff GJ, van der Voort HT, van Spronsen EA, Nanninga N. Three-dimensional imaging by confocal scanning fluorescence microscopy. *Ann. N.Y. Acad. Sci.* 1986;**483**:405-15.
- Carlsson K. Three-dimensional microscopy using a confocal laser scanning microscope. *Optics Letters* 1985;**10**:53-55.

Received 6 August 2004. Accepted 16 August 2004.

©M.B. Cannell 2004.

Author for correspondence:

M.B. Cannell

Department of Physiology,  
School of Medical Sciences,  
The University of Auckland,  
Auckland, New Zealand

Tel: +64 9373 7599 x86201

Fax: +64 9373 7499

E-mail: m.cannell@auckland.ac.nz

## Development of low affinity, membrane targeted $\text{Ca}^{2+}$ sensors suitable for measuring presynaptic $\text{Ca}^{2+}$

M. Monif, M.L. Smart, C.A. Reid & D.A. Williams

Department of Physiology,  
The University of Melbourne,  
Grattan St, Parkville,  
Melbourne, 3010, Australia

### Summary

1. Our aim is to measure near-membrane  $\text{Ca}^{2+}$  flux within presynaptic terminals of central neurons by modifying new genetically encoded  $\text{Ca}^{2+}$  sensors to develop tools capable of measuring localised  $\text{Ca}^{2+}$  signals.

2. We used standard recombinant DNA technologies to generate the DNA coding for a fusion construct of a modified fluorescent "pericam"  $\text{Ca}^{2+}$  biosensor with a presynaptic P2X7 receptor (P2X7R). The  $\text{Ca}^{2+}$  sensitivity of the biosensor was modified by rational site-directed mutagenesis of the calmodulin portion of the pericam.

3. Biosensor-receptor fusions were transfected into expression systems for evaluation. Expression studies in Human Embryonic Kidney-293 (HEK-293) cells showed that biosensor-receptor fusion construct delivered protein was localised exclusively to the plasma membrane, confirming that fusion did not affect the ability of the receptor to undergo normal protein synthesis and trafficking.

4. The  $\text{Ca}^{2+}$ -dependent fluorescence of the pericam portion of the fusion protein was also retained. Site-direct mutagenesis within the calmodulin moiety of the pericam significantly reduced the  $\text{Ca}^{2+}$  affinity of the complex. The dynamic range of the sensor following this modification is better matched to the higher  $\text{Ca}^{2+}$  levels expected within presynaptic  $\text{Ca}^{2+}$  micro-domains.

### Introduction

$\text{Ca}^{2+}$  is a ubiquitous cellular messenger controlling a diverse array of physiological processes from fertilisation through to gene transcription, muscle contraction, cell proliferation and migration, cell differentiation and ultimately, cell death. Tight control of the spatial, temporal and concentration profile of  $\text{Ca}^{2+}$  influx is therefore required to define specific functional roles in cells. This is important in the neuronal setting, especially within the presynaptic terminal where the release of transmitter is critically dependent upon small changes in  $\text{Ca}^{2+}$  concentrations<sup>1</sup>. The invasion of an action potential into the presynaptic terminal opens voltage-dependent  $\text{Ca}^{2+}$  channels allowing the rapid influx of  $\text{Ca}^{2+}$  ions, giving rise to a small local volume (microdomain) of elevated  $\text{Ca}^{2+}$ <sup>2-4</sup>.  $\text{Ca}^{2+}$  microdomains coincide with active zones that are areas of presynaptic membrane densely packed with  $\text{Ca}^{2+}$  channels and docked with neurotransmitter vesicles<sup>3</sup>. At these microdomains the  $\text{Ca}^{2+}$  concentration reaches

approximately  $100\mu\text{M}$ <sup>5</sup> within 800 microseconds<sup>6</sup>, over distances of less than  $1\mu\text{m}$  from the point of entry<sup>7</sup>.  $\text{Ca}^{2+}$  microdomains are determinants of neurotransmitter release<sup>2</sup> and play an important role in the modulation of synaptic strength<sup>8</sup>. Historically, it has been a challenging exercise to measure  $\text{Ca}^{2+}$  microdomains due to their small spatio-temporal profiles, with the most reliable data derived from modelling and simulation studies<sup>9</sup>. The difficulty in measuring  $\text{Ca}^{2+}$  microdomains means that a wide range of  $\text{Ca}^{2+}$ -specific signalling processes may go undetected by the current 'volume-averaged' methods routinely used. There is clearly a need for a biosensor that is capable of sensing  $\text{Ca}^{2+}$  microdomains. Genetically encoded  $\text{Ca}^{2+}$  sensors based on green fluorescent protein (GFP) provide an exciting opportunity to develop tools to measure these localised signals.

GFP derived from *Aequorea Victoria* jelly fish is a 238 amino acid protein with an apparent molecular weight of 27-30kDa<sup>10</sup>. Several GFP mutants with distinct spectral qualities have been established as sensors of cellular dynamics, for example, in monitoring local pH or  $\text{Ca}^{2+}$  concentration inside cells<sup>11</sup>. A powerful example of this technology has been the recent development of pericams<sup>12</sup> that consist of a single GFP variant sensitive to physiologically relevant substrates such as  $\text{Ca}^{2+}$  ions. To construct the pericams, circularly permuted enhanced yellow fluorescent proteins (cpEYFP) were used in which the amino and carboxyl portions had been interchanged and reconnected by a short spacer between the original termini. Calmodulin was fused to the C terminus of cpEYFP and its target peptide, M13, to the N terminus. The pericam was shown to be fluorescent with its spectral properties changing reversibly with the amount of  $\text{Ca}^{2+}$ . Of the three major pericams developed, ratiometric-pericam (RP) appeared to be most promising, in that due to its capacity for dual excitation nature, it has potential for quantitative imaging.

Insertions of genetically encoded sensor into host receptors that already have localisation signals offers a new strategy for measuring localised  $\text{Ca}^{2+}$ . Our goal is to measure  $\text{Ca}^{2+}$  microdomains within presynaptic terminals. The requirement therefore is a receptor that localises to the presynaptic membrane, but does not play a critical role in evoked release. The P2X7Rs are ligand-gated ion channels that are gated by ATP and other nucleotides<sup>13-15</sup>. Studies of expression patterns of P2X7R have confirmed localisation in presynaptic nerve terminals in both central and peripheral neurons<sup>16</sup>. Further, immunoreactivity studies in the

hippocampus indicate that P2X7Rs colocalise with the vesicular glutamate transporter, (VGLUT1), placing them within excitatory terminals<sup>17</sup>. This makes P2X7R an ideal tool for targeting  $Ca^{2+}$  sensors to excitatory presynaptic nerve terminals in the hippocampus. Smart and colleagues have revealed that fusion of the purinergic P2X7R to GFP directed the complex to the plasma membrane in the simple HEK expression system<sup>18</sup>. Here we use this simple expression system to characterise a RP-P2X7R construct, determining its trafficking and  $Ca^{2+}$  sensing ability.

As  $Ca^{2+}$  concentrations within the presynaptic microdomains are thought to be in the 50-100 $\mu$ M range, the dissociation constant (Kd) of RP, reported to be 1.7 $\mu$ M, is therefore lower than required. As part of fine-tuning the  $Ca^{2+}$  affinities of a previous  $Ca^{2+}$  sensor, cameleons<sup>19</sup>, a number of mutations were performed in the calmodulin moiety of this construct to optimise the Kd for this reporting range. In particular a substitution mutation in the first  $Ca^{2+}$  binding loop of calmodulin, where the 31<sup>st</sup> amino acid was changed from glutamic acid (E) to glutamine (Q), shifted the titration curve of cameleon-1 to the right reflecting an increase in the Kd of its low affinity component from 11 $\mu$ M to 700 $\mu$ M<sup>19</sup>. Here we use a similar strategy to lower the affinity of the RP, making it more suitable for measuring the high  $Ca^{2+}$  concentrations expected in presynaptic microdomains.

## Methods

### Gene construction

To incorporate the E31Q mutation into RP a total of three PCR reactions were performed. First the cDNA of the 5' portion of RP(E31Q) was amplified with a sense primer containing a HindIII restriction site and a reverse primer 5' C GGT GCC AAG TT G CTT TGT GGT GAT GG (with the base change introducing the mutation of interest being underlined). For both RP and RP(E31Q) a glycine-rich spacer sequence, GGA GGT GCA GGT AGT GGA GGT corresponding to Gly-Gly-Ala-Gly-Ser-Gly-Gly, was included upstream of the start codon in the forward primer. In the second PCR reaction, the cDNA of the 3' portion of RP(E31Q) was amplified with a forward primer: 5'CC ATC ACC ACA AAG C AA CTT GGC ACC G, and a reverse primer containing a XhoI restriction site. Finally the entire cDNA of RP(E31Q) was amplified with the HindIII and XhoI sites containing primers by using a mixture of the first and second PCR fragments as the template. The restricted product was cloned in-frame into the HindIII/XhoI sites of pcDNA3.1 (Invitrogen) vector. To generate the chimeric sensors, P2X7R-RP and P2X7R-RP(E31Q), a subcloning strategy was employed. The cDNA encoding P2X7R was amplified by using primers containing 5'NheI and 3'HindIII restriction sites. The restricted PCR fragments were ligated to the 5' end of RP or RP(E31Q) gene in pcDNA3.1 to yield the tagged  $Ca^{2+}$  sensor constructs of P2X7R-RP and P2X7R-RP(E31Q).

### In vitro spectroscopy

To assess the spectral characteristics of the RP and RP(E31Q) proteins, HEK-293 cells were transfected with each DNA construct using Lipofectamine<sup>TM</sup>2000 (Life Technologies). Transfected HEK-293 cells were lysed 3 days post transfection and liberated cytosolic proteins (RP and RP(E31Q)) were collected. To determine the Kds of RP and RP(E31Q), a  $Ca^{2+}$  Calibration Buffer Kit (Molecular Probes, C-3009) was used. The spectral properties of the proteins were measured using a Hitachi F-4010 Fluorescence Spectrophotometer. In separate experiments RP and RP(E31Q) were excited at 480nm, with an emission wavelength scan performed from 480 to 650nm. The solutions were maintained at pH 7.20 and 24°C. The Kd of both indicators (RP and RP(E31Q)) was calculated from a linearised (Hill) plot of fluorescence intensity as a function of  $Ca^{2+}$  concentration. Data were generated by scanning the emission spectrum of the indicator in the presence of different  $Ca^{2+}$  concentrations. All data for RP or RP(E31Q) were corrected for the fluorescence or a reference solution containing non-transfected HEK-293 cells (autofluorescence).

### Imaging

Fluorescence-based approaches were used to characterise the  $Ca^{2+}$  sensors. Two or three days after cDNA transfection with Lipofectamine<sup>TM</sup>2000, HEK-293 adherent on poly-L-lysine-coated coverslips were analysed microscopically. Cells bathed in HEPES buffer (mM: NaCl 147, KCl 2, HEPES 10, Glucose 10,  $CaCl_2$  1 pH: 7.4) were imaged at 24°C on a laser scanning confocal (Biorad MRC-1024ES) employing an argon-ion laser, coupled to a Nikon Diaphot 300 microscope. Both the tagged and untagged RPs were illuminated at 488 nm, which excited the YFP portion of the constructs. YFP fluorescence emission of the RP was collected through a 510 long pass dichroic mirror and OG515 emission filter (>515nm). Fluorescence distribution patterns of tagged and untagged biosensors were achieved by collecting 512x512 pixel confocal images (slow scan rate – 1 s/image), a bright field or transmitted image, and a simultaneous image showing the colocalisation of the confocal signal with the transmitted image which revealed fluorescent cellular structures. Some images were taken as an average of 4 consecutive scans (Kalman algorithm) to smooth random noise fluctuations. For assessment of the  $Ca^{2+}$  sensing ability of the  $Ca^{2+}$  sensors the acquisition package 'Timecourse' was used. In any given field of cells several regions of interest (ROI) were defined. Examination of the  $Ca^{2+}$  sensing properties of the RP, RP(E31Q) or chimeric constructs was performed in transfected HEK-293 cells being exposed to 2.5 $\mu$ M ionomycin (Sigma).

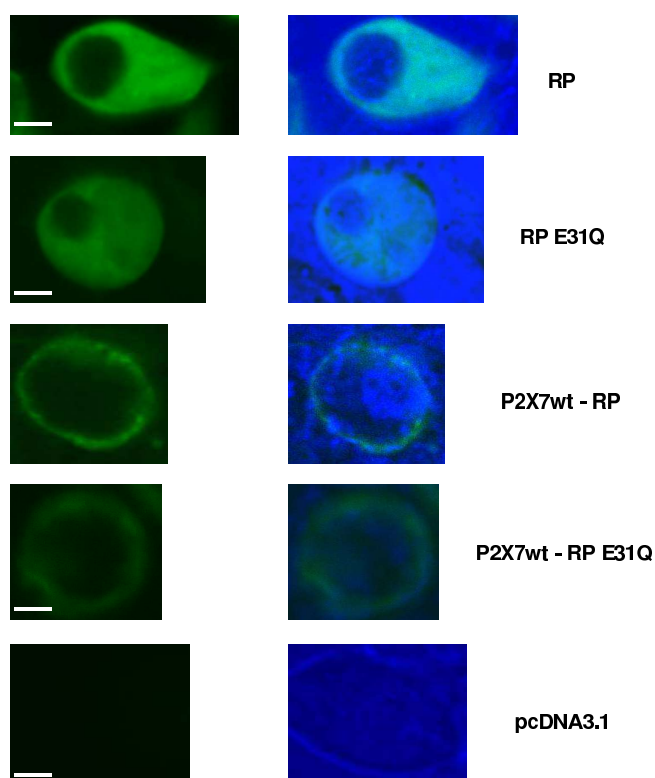


**Figure 1. Sub-cellular localisation of tagged and untagged  $Ca^{2+}$  sensor constructs expressed in HEK-293 cells.**

Images were captured using a laser scanning confocal microscope (488 excitation,  $>510$  emission). Left panel represents the fluorescence images, displayed at identical gain and black level settings. Right panel is the co-registration of the fluorescence image with transmission light image of the same field. Transmission light images reveal the cell outline and presence of organelles. Scale bar =  $5\mu\text{m}$ .

**A** Ratiometric Pericam (RP)

**B** Ratiometric Pericam E31Q (RP(E31Q))

**C** P2X7R-RP

**D** P2X7R-RP(E31Q)

**E** pcDNA3.1 vector (control) which shows no fluorescence

## Results and Discussion

### Development of a near-membrane $Ca^{2+}$ sensor

A fusion between a ratiometric pericam and a membrane targeted protein, the P2X7R was carried out using standard molecular biology techniques. This was revealed by imaging HEK-293 cells transfected with either the tagged (localised) or untagged (unlocalised) pericams and comparing fluorescence distribution patterns. As expected, untagged ratiometric pericams (RP) displayed a bright fluorescence intensity, which was confined to the cytosol but excluded from the nucleus (Figure 1A). Our targeting strategy of fusing the RP to P2X7R was tested next. P2X7R-GFP is known to localise to the plasma

membrane in the HEK expression system<sup>18</sup>. P2X7R-RP exhibits an identical expression pattern (Figure 1C) to that of P2X7R-GFP, suggesting that the normal P2X7R trafficking is not disrupted by the addition of RP. The signal sequence on the P2X7R therefore directed the ratiometric pericams exclusively to the plasma membrane. Confirming the locality of the sensors provides us with the potential for exclusively reporting near-membrane  $Ca^{2+}$  signals.

### Fine-tuning the $K_d$ of ratiometric pericams to measure high $Ca^{2+}$ concentrations

The high affinity of RP makes it unsuitable to accurately measure the large  $Ca^{2+}$  flux expected at presynaptic microdomains. Site-directed mutagenesis within the calmodulin portion of the  $Ca^{2+}$  sensor, cameleon-1, shifts the fluorescence- $Ca^{2+}$  relationship<sup>19</sup>. A single glutamic acid to glutamine mutation (RP(E31Q)) weakens the interaction between  $Ca^{2+}$  and its binding loop, decreasing the affinity of the sensor and increasing its dynamic range<sup>19</sup>. The mutation was introduced using a standard PCR protocol and it was confirmed by direct sequencing. RP and RP(E31Q) displayed virtually identical emission spectra, with an emission maximum at approximately 515nm, coinciding with the emission peak of the YFP portion of each pericam (Figure 2A). This observation confirms that the E31Q mutation did not alter the spectral characteristics of the protein. The E31Q mutation in RP altered the  $K_d$  from  $2.1\mu\text{M}$  to  $19.1\mu\text{M}$  effectively improving the dynamic range of  $0.25\mu\text{M}$ - $19\mu\text{M}$  to approximately  $2\mu\text{M}$ - $170\mu\text{M}$  (Figure 2B). RP(E31Q) expressed in HEK cells is uniformly distributed through the cytoplasm, but is excluded from the nucleus (Figure 1B). The P2X7R-RP(E31Q) construct was also generated and displayed an identical expression pattern to P2X7R-RP, limited to the plasma membrane (Figure 1D). The lower fluorescent signal seen with RP(E31Q) is consistent with its lower  $Ca^{2+}$  affinity (Figure 1C,D).

### Will the sensors be sensitive enough to measure $Ca^{2+}$ microdomains?

In turtle hair cells the  $Ca^{2+}$  concentration in  $Ca^{2+}$  microdomains was found to be at least  $85\mu\text{M}$ <sup>7</sup>. Others have reported microdomain  $Ca^{2+}$  concentrations of  $100$ - $200\mu\text{M}$ , necessary to produce rapid neurotransmitter secretion<sup>5</sup>. With a dynamic range of  $0.25\mu\text{M}$ - $19\mu\text{M}$  the original RP indicator would be expected to saturate at these high concentrations. However, the RP(E31Q), with a dynamic range of  $2\mu\text{M}$ - $171\mu\text{M}$ , is ideally suited to the expected levels of  $Ca^{2+}$  concentrations within presynaptic microdomains.

### Sensing $Ca^{2+}$ in a mammalian expression system using genetically encoded sensors

HEK-293 cells transfected with each pericam were exposed to the ionophore ionomycin ( $2.5\mu\text{M}$ ). Both the P2X7R-RP and P2X7R-RP(E31Q) sensors demonstrated an

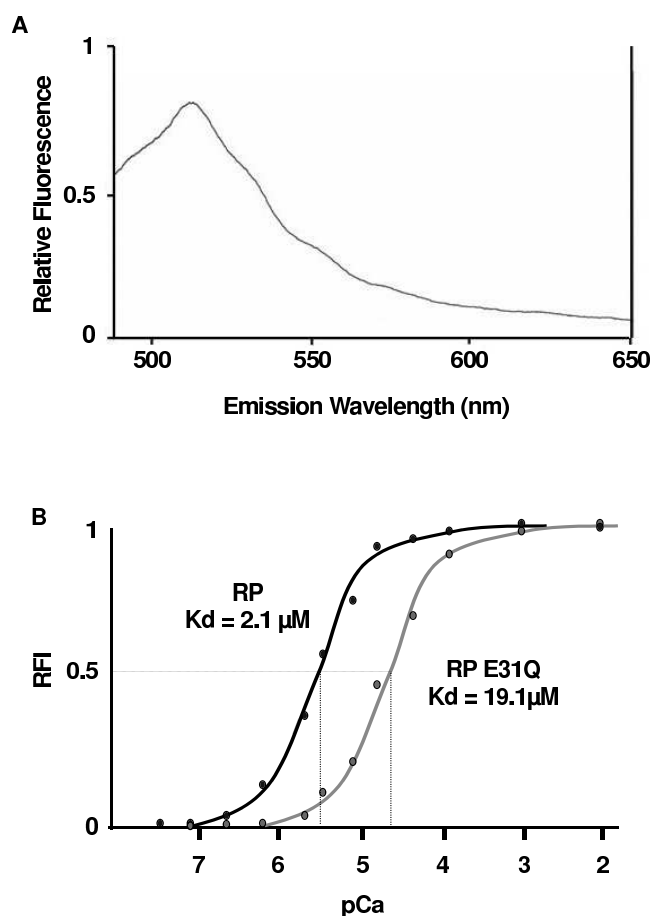


**Figure 2. In-vitro properties of ratiometric pericams.**

**A** Fluorescence emission spectrum of ratiometric pericam E31Q (RP(E31Q)). HEK-293 cells transfected with RP(E31Q) were lysed and the liberated cytosolic proteins containing RP(E31Q) were diluted in phosphor-buffered saline (PBS). Emission wavelength scans (490nm-650nm) were obtained using a spectrophotometer. The spectrum was measured at 24°C and pH 7.20, and the results corrected for with a reference solution identical in composition to the sample except for the absence of RP(E31Q). The results were similar to YFP spectra, showing an emission peak at approximately 515nm. A very similar emission spectrum was obtained for RP (results not shown) with a maximum peak at 510nm, indicating the maintenance of YFP spectral properties.

**B** Dose response curves of ratiometric pericams, showing relative fluorescence intensity (RFI) as a function of pCa ( $-\log_{10}[\text{Ca}^{2+}]_{\text{free}}$ ). The curves were generated by scanning the emission of the indicator (RP or RP(E31Q)) at 515nm. The concentration of free  $\text{Ca}^{2+}$  ions in solution was varied by cross dilution of  $\text{Ca}^{2+}$  ("high  $\text{Ca}^{2+}$  solution") and EGTA ("low  $\text{Ca}^{2+}$  solution") to produce a series of eleven solutions with increasing  $[\text{Ca}^{2+}]$  while keeping the concentration of the indicator (RP or RP(E31Q)) constant. The pH was kept at 7.2 during experimentation. The E31Q mutation shifted the dose response curve to the right, reflecting a change in Kd from 2.1 $\mu\text{M}$  for RP to 19.1 $\mu\text{M}$  for RP(E31Q).

increase in fluorescence intensity in response to application of ionomycin (Figure 3). As expected, P2X7R-RP showed a significantly larger change in fluorescence intensity than the lower affinity sensor, P2X7-RP(E31Q). These experiments demonstrate that the  $\text{Ca}^{2+}$  sensing abilities of the RP and RP(E31Q) are not altered when fused to the P2X7R and expressed in a mammalian cell line. Further studies are required to demonstrate this in primary neuronal cultures and other neuronal preparations.

*Will the sensor only measure  $\text{Ca}^{2+}$  from presynaptic  $\text{Ca}^{2+}$  microdomains?*

Using simulation studies, Fogelson and colleagues<sup>9</sup> predicted with a three dimensional model that  $\text{Ca}^{2+}$  enters the presynaptic terminal through discrete membrane channels and acts to release transmitter within 50nm of the entry point. In turtle hair cells the initial diameter of  $\text{Ca}^{2+}$  microdomains was found to be less than 1  $\mu\text{m}$ , as estimated by confocal microscopy<sup>7</sup>. Hence,  $\text{Ca}^{2+}$  microdomains can have very restricted spatial profiles and restricting even a sensor to the membrane may not guarantee localisation within  $\text{Ca}^{2+}$  microdomains (e.g. in neurons). However, one could still expect much better signal-to-noise ratios with a

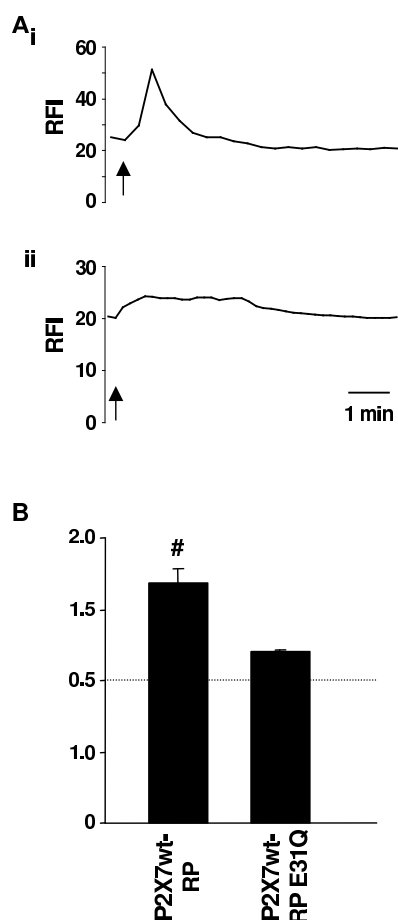


**Figure 3. Responses of chimeric  $\text{Ca}^{2+}$  sensor constructs when expressed in HEK-293 cells to  $2.5 \mu\text{M}$  ionomycin.**

**A** Typical responses of HEK-293 cells expressing: (i) P2X7R-RP, (ii) P2X7R-RP(E31Q) upon application of ionomycin ( $2.5 \mu\text{M}$ ) as indicated by the upward arrows below each trace. RFI indicates relative fluorescence intensity. Application of ionomycin caused a transient increase in relative fluorescence intensity in each case, but the response of P2X7R-RP(E31Q) was smaller as compared to the response of P2X7R-RP. All experiments were performed in HEPES solution containing  $1 \text{mM}$   $\text{CaCl}_2$ . For each trace the horizontal bar indicates 1 minute.

**B** Collated responses of HEK-293 cells expressing each of the chimeric  $\text{Ca}^{2+}$  sensor constructs, P2X7R-RP ( $n=13$  cells), P2X7R-RP(E31Q) ( $n=9$  cells) to  $2.5 \mu\text{M}$  ionomycin.  $F/F_0$  indicates peak fluorescence intensity over basal fluorescence intensity. Responses are expressed as mean  $F/F_0 \pm$  s.e.m. #  $P < 0.05$  (one-way Anova) significantly different to P2X7R-RP(E31Q).

membrane-delimited sensor as opposed to a generalised cytosolic sensor. Therefore, a localised biosensor responding selectively to  $\text{Ca}^{2+}$  signals near the presynaptic membrane will provide a valuable tool to more accurately measure these signals. Further experiments will determine how close we can get.

## Conclusion and Future Directions

The  $\text{Ca}^{2+}$  microdomains within presynaptic nerve terminals are highly localised and the concentrations of  $\text{Ca}^{2+}$  within these regions are thought to be significantly larger than the global cytosolic concentration. By measuring 'volume-averaged' global signals in response to stimuli, important information about these compartmentalised functions remains undetected. In this study biosensors have been designed with characteristics suited to investigating  $\text{Ca}^{2+}$  microdomains within presynaptic terminals. We generated a fusion protein of a ratiometric pericam (with modified  $\text{Ca}^{2+}$ -sensing ability) and a P2X7 receptor, a protein known to localise to the presynaptic membrane of excitatory neurons. Fusion proteins successfully trafficked to the plasma membrane distribution of HEK cells and were capable of responding to changes in intracellular  $\text{Ca}^{2+}$ . Our next goal is to characterise these sensors in a neuronal setting, confirming localisation and  $\text{Ca}^{2+}$  sensing ability and refining these properties where necessary. Ultimately, we hope to study  $\text{Ca}^{2+}$  dynamics in brain slices derived from various mouse and rat models of relevant human diseases. The generation of genetically encoded fluorescent biosensors described is expected to continue to expand and provide exciting new insights into normal physiological and pathological processes in neurons.

## Acknowledgments

Supported by funding from NHMRC and ARC (Australia). We are grateful for the careful proofreading of Samantha Ferguson.

## References:

1. Reid CA, Bekkers JM, Clements JD. N- and P/Q-type  $\text{Ca}^{2+}$  channels mediate transmitter release with a similar cooperativity at rat hippocampal autapses. *J. Neurosci.* Apr 15 1998;18(8):2849-2855.
2. Augustine GJ. How does calcium trigger neurotransmitter release? *Curr Opin Neurobiol.* Jun 2001;11(3):320-326.
3. Llinas R, Sugimori M, Silver RB. Microdomains of high calcium concentration in a presynaptic terminal. *Science.* May 1 1992;256(5057):677-679.
4. Jarvis SE, Zamponi GW. Interactions between presynaptic  $\text{Ca}^{2+}$  channels, cytoplasmic messengers and proteins of the synaptic vesicle release complex. *Trends Pharmacol Sci.* Oct 2001;22(10):519-525.
5. Heidelberger R, Heinemann C, Neher E, Matthews G. Calcium dependence of the rate of exocytosis in a synaptic terminal. *Nature.* Oct 6 1994;371(6497):513-515.
6. Sugimori M, Lang EJ, Silver RB, Llinas R. High-resolution measurement of the time course of calcium-concentration microdomains at squid presynaptic terminals. *Biol. Bull.* Dec 1994;187(3):300-303.
7. Tucker T, Fettiplace R. Confocal imaging of calcium

- microdomains and calcium extrusion in turtle hair cells. *Neuron*. Dec 1995;15(6):1323-1335.
8. Zucker RS. Calcium- and activity-dependent synaptic plasticity. *Curr Opin Neurobiol*. Jun 1999;9(3):305-313.
  9. Fogelson AL, Zucker RS. Presynaptic calcium diffusion from various arrays of single channels. Implications for transmitter release and synaptic facilitation. *Biophys. J*. Dec 1985;48(6):1003-1017.
  10. Tsien RY. The green fluorescent protein. *Annu. Rev. Biochem.* 1998;67:509-544.
  11. Gerdes HH, Kaether C. Green fluorescent protein: applications in cell biology. *FEBS Lett*. Jun 24 1996;389(1):44-47.
  12. Nagai T, Sawano A, Park ES, Miyawaki A. Circularly permuted green fluorescent proteins engineered to sense Ca<sup>2+</sup>. *Proc. Natl. Acad. Sci. USA*. Mar 13 2001;98(6):3197-3202.
  13. North RA, Surprenant A. Pharmacology of cloned P2X receptors. *Annu. Rev. Pharmacol. Toxicol.* 2000;40:563-580.
  14. Paukert M, Hidayat S, Grunder S. The P2X(7) receptor from *Xenopus laevis*: formation of a large pore in *Xenopus* oocytes. *FEBS Lett*. Feb 27 2002;513(2-3):253-258.
  15. Rassendren F, Buell GN, Virginio C, Collo G, North RA, Surprenant A. The permeabilizing ATP receptor, P2X7. Cloning and expression of a human cDNA. *J. Biol. Chem.* Feb 28 1997;272(9):5482-5486.
  16. Deuchars SA, Atkinson L, Brooke RE, et al. Neuronal P2X7 receptors are targeted to presynaptic terminals in the central and peripheral nervous systems. *J Neurosci*. Sep 15 2001;21(18):7143-7152.
  17. Atkinson L, Batten TF, Moores TS, Varoqui H, Erickson JD, Deuchars J. Differential co-localisation of the P2X7 receptor subunit with vesicular glutamate transporters VGLUT1 and VGLUT2 in rat CNS. *Neuroscience*. 2004;123(3):761-768.
  18. Smart ML. Molecular Basis of P2X7R Pore Formation (Thesis). The laboratory of Biophysics and Molecular Biology. Department of Physiology, The University of Melbourne. 2002.
  19. Miyawaki A, Llopis J, Heim R, et al. Fluorescent indicators for Ca<sup>2+</sup> based on green fluorescent proteins and calmodulin. *Nature*. Aug 28 1997;388(6645):882-887.

Author for correspondence:

Prof. David A. Williams  
Department of Physiology  
The University of Melbourne  
Grattan St,  
Melbourne, Vic 3010  
Australia

Tel: +61 3 8344 5845

Fax: +61 3 8344 5818

Email: davidaw@unimelb.edu.au

Received 8 June 2004, in revised form 30 June 2004.

Accepted 3 July 2004.

©D.A. Williams 2004.

## Functional imaging: new views on lens structure and function

Paul J. Donaldson, Angus C. Grey, B. Rachele Merriman-Smith, A.M.G. Sisley,  
Christian Soeller, Mark B. Cannell & Marc D. Jacobs

*Department of Physiology, School of Medical Sciences,  
The University of Auckland, Auckland, New Zealand*

### Summary

1. We have developed an experimental imaging approach that allows the distribution of lens membrane proteins to be mapped with subcellular resolution over large distances, as a function of fibre cell differentiation.

2. Using this approach in the rat lens, we have precisely localised histological sites of Cx46 cleavage, quantitatively mapped changes in gap junction distribution and fibre cell morphology, and correlated these changes to differences in intercellular dye transfer.

3. Profiling of glucose transporter isoform expression showed that lens epithelial cells express GLUT1 while deeper, cortical fibre cells express the higher-affinity GLUT3 isoform. Near the lens periphery, GLUT3 was located in the cytoplasm of fibre cells, but it underwent a differentiation-dependent membrane insertion.

4. Similarly, the putative adhesion protein MP20 is inserted into the fibre cell membranes, at the stage when the cells lose their nuclei. This redistribution is strikingly rapid in terms of fibre cell differentiation and correlates with a barrier to extracellular diffusion.

5. Our imaging-oriented approach has facilitated new insights into the relationships between fibre cell differentiation and lens function. Taken together, our results indicate that a number of strategies are utilised by the lens during the course of normal differentiation, to change the subcellular distribution, gross spatial location and functional properties of key membrane transport proteins.

### Introduction

The transparency of the lens is closely linked to the unique structure and function of its fibre cells. These highly differentiated cells are derived from equatorial epithelial cells, which exit the cell cycle and embark upon a differentiation process that produces extensive cellular elongation, the loss of cellular organelles and nuclei and the expression of fibre-specific proteins<sup>1,2</sup>. Since this process continues throughout life, a gradient of fibre cells at different stages of differentiation is established around an internalised core of mature, anucleate fibre cells. To maintain its structural organization, and hence, its transparency, the lens is believed to have an internal microcirculation system that delivers nutrients, removes waste products, and imposes the negative membrane potential required to maintain the steady-state volume of the

fibre cells<sup>3</sup>. This system is thought to be generated by spatial differences in ion transport processes that generate a circulating flux of ions which enters the lens via the extracellular clefts between fibre cells, crosses fibre cell membranes, then flows from cell to cell towards the surface of the lens, via an intracellular pathway mediated by gap junction channels. This circulating current creates a net flux of solute that generates fluid flow. The extracellular flow of water conveys nutrients toward the deeper-lying fibre cells, while the intracellular flow removes wastes and creates a well-stirred intracellular compartment.

The experimental evidence in support of this model of lens circulation has primarily been provided by macroscopic measurements of whole-lens electrical properties<sup>3</sup>. More recently, our laboratory has provided additional evidence in favour of the model by identifying, and localising at the cellular level, key components of the circulation system<sup>4</sup>. This work has involved a number of functional imaging approaches which correlate membrane protein distribution to function in spatially distinct regions of the lens<sup>5-8</sup>. Here we compare and contrast the results obtained for three diverse types of membrane proteins: cell-to-cell channel proteins (connexins); glucose transporter proteins (GLUTs); and an adhesion protein (MP20). While our initial goal was to provide a molecular inventory of key components of the lens circulation system, our results have revealed that the lens uses a number of different strategies to establish and maintain spatial differences in membrane transport proteins during the course of fibre cell differentiation.

### *Mapping spatial differences in transport proteins: a question of scale*

To investigate these questions we have developed an experimental approach that allows the distribution of lens membrane proteins to be mapped with subcellular resolution over large distances. Since fibre cells continually differentiate from epithelial cells at the lens periphery and are progressively internalised with age, the spatial layout of fibre cells from the lens periphery to the centre also represents a temporal profile of fibre cell differentiation. The technical procedures we have developed<sup>9</sup> to map membrane protein distributions across this differentiation gradient, utilize high-quality cryosections that are systematically imaged to produce a continuous, high-resolution data set (Figure 1). Such an image data set contains information not only on how the gross spatial distribution of a labeled membrane protein changes as a

function of fibre cell differentiation, but also on the changing subcellular distribution of the protein (Figure 2). This is important because differentiating fibre cells are essentially elongated epithelial cells, which retain distinct apical, basal and lateral membrane domains<sup>10</sup>. In these cells the lateral membranes are further divided into broad and narrow sides, which contribute to the distinctive hexagonal profile of the fibre cells. Thus in addition to radial differences in membrane protein distribution which can occur as a consequence of fibre cell differentiation, other changes may be evident in an axial direction (pole-equator-pole) along the length of a fibre cell or between the lateral membrane domains (broad versus narrow side).

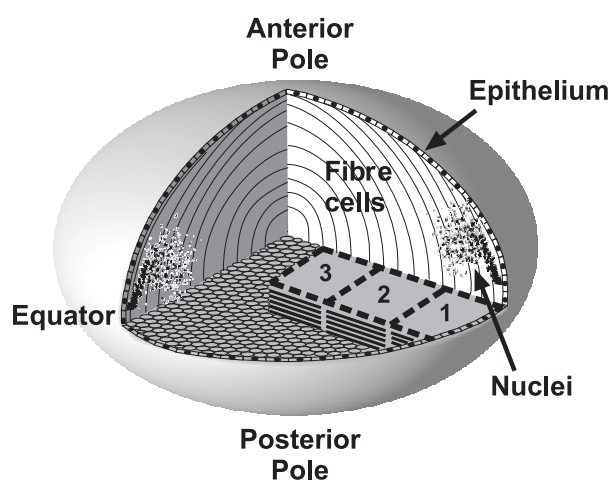


**Figure 1. High-resolution long-range imaging in the lens.** This diagram illustrates our application of quantitative two-photon, and confocal imaging in the equatorial region of the lens. Overlapping, large image stacks (1-3) can be collected from high-quality cryosections at diffraction-limited resolution, and precisely aligned by correlation analysis<sup>9</sup> to form a continuous 3D data set spanning a large proportion of the lens radius (see Figure 2). Expression patterns of immunofluorescence-labeled proteins can be examined qualitatively by extracting high-magnification views from exact locations within the data set, or analyzed quantitatively as a function of fibre cell age using custom-written image processing software. Fibre cell nuclei disperse axially (i.e. toward the poles) and degrade as the cells age, providing a convenient differentiation marker when stained with a DNA-binding fluorochrome such as propidium iodide. Nuclear degradation, and protein expression in fibre cell lateral membrane domains, can be precisely localised in equatorial sections showing transverse views of fibre cells. Nuclear dispersal, degradation and longitudinal protein expression patterns, can be localised in axial sections showing the fibre cell lengths.

#### *Fibre cell gap junctions: structure, dispersal and age-dependent processing*

Because of their central importance to lens function, the fibre cell gap junctions have been extensively studied<sup>11</sup>. Gap junctions are formed by the connexin family of proteins<sup>12</sup> and lens fibre cells express two connexin isoforms, Cx46<sup>13</sup> and Cx50<sup>14</sup>. Functional studies indicate that the density of gap junctions is highest near the equator of the lens so as to direct the outward component of the circulating current to the equatorial epithelial cells, which contain the highest density of Na/K pumps<sup>15</sup>. Qualitative assessments showed that in the young, equatorial fibre cells, gap junctions are particularly concentrated on the broad sides while in older, inner fibre cells, the gap junctions are more evenly distributed throughout the cell membrane.<sup>16-18</sup> Furthermore, biochemical studies have shown that the cytoplasmic tails of Cx46<sup>19</sup> and Cx50<sup>20,21</sup> are cleaved in the lens, the latter by the protease calpain<sup>21</sup>, in order to maintain cell coupling at low pH deep in the lens<sup>22</sup>.

In a more recent study which utilised our high-resolution imaging techniques, we have precisely localised the histological sites of Cx46 cleavage, by quantitative analysis of signal density profiles obtained from antibodies directed against the cytoplasmic loop and tail of Cx46<sup>8</sup>. Our analysis revealed that Cx46 cleavage occurs at two distinct stages during fibre cell differentiation (Figure 3A). The major stage occurs at a normalized radial distance ( $r/a$ )  $\sim 0.9$  in 3-week-old lenses, and coincides with an axial dispersal of fibre cell nuclei; the second stage occurs at  $r/a \sim 0.7$  and is associated with the complete loss of fibre cell nuclei.

In addition to Cx46 cleavage, we have quantitatively mapped the changing gap junction distributions (Figure 2A-C) as a function of fibre cell differentiation. Radial changes in cell shape and gap junction plaque size and distribution were measured automatically by quantitative morphometric analysis of our image data<sup>8</sup>. A fibre cell 'ellipticity index' was found to increase smoothly from the lens periphery inward, reflecting a gradual change from the hexagonal peripheral cell cross-section to a more circular cross-section. We also quantified a rapid peripheral decrease in the size of broad side plaques which is followed by an apparent fragmentation and dispersal of the plaques around the cell perimeter. These precise radial measurements of fibre cell changes show that the sudden gap junction cleavage and shrinkage events do not correspond to sudden changes in cellular morphology. However, the loss of the hexagonal cell profile is closely associated with gap junction plaque dispersal, and both follow the major stage of Cx46 cleavage, suggesting a possible role for cleavage in gap junction and cell remodeling<sup>8</sup>.

To investigate the functional consequences of these changes, we performed two-photon flash photolysis (TPFP) on lenses loaded with CMNB-caged fluorescein and assessed regional gap junction coupling patterns<sup>8</sup>. By applying TPFP inside a single fibre cell, a microscopic source of uncaged fluorescein was created and its diffusion to neighbouring cells was monitored by simultaneous

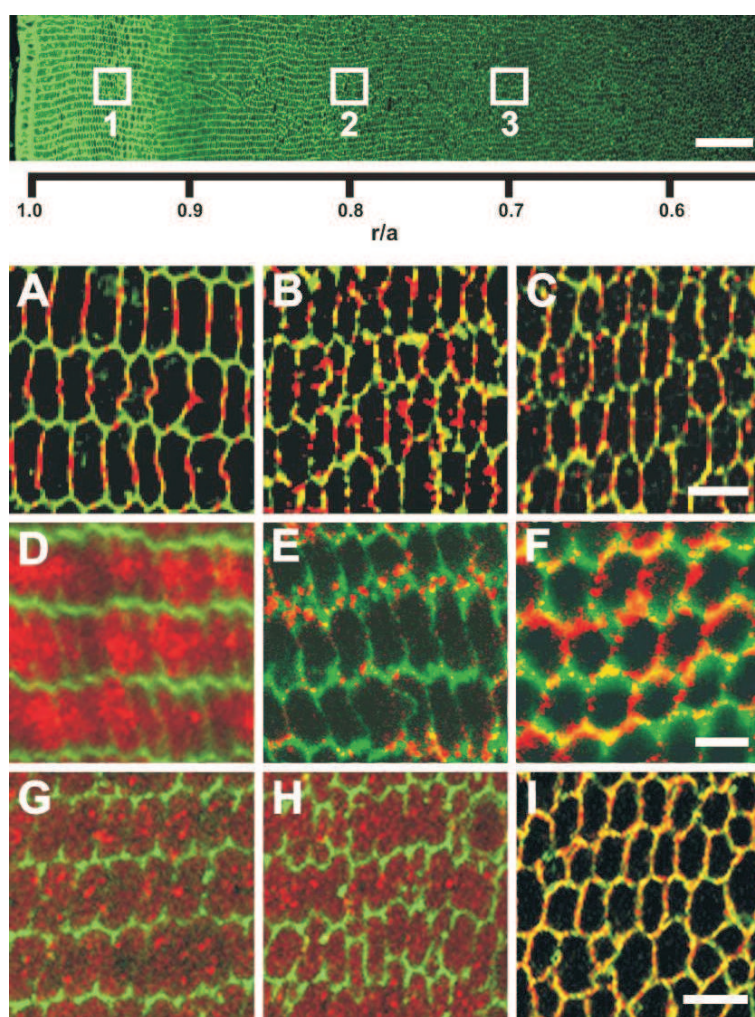


**Figure 2. Differentiation-dependent changes in the subcellular distribution of 3 diverse lens proteins.**

Top: Four 1024 x 1024 image stacks were assembled as described (Figure 1) to form a continuous, high-resolution immunofluorescence data set extending over half the rat lens radius. The image shows cell membranes labeled with wheat germ agglutinin conjugated to AlexaFluor 350. High-magnification images of the proteins (A-I) were extracted from the approximate locations designated with white boxes to view changes in their distribution as a function of fibre cell age.

A-C: The gap junction protein Cx46 forms large plaques on the broad sides of fibre cells near the lens periphery, with small punctate plaques on the narrow sides (A). As fibre cells age they become rounder, the large plaques become smaller (B), and they fragment and disperse around the cell membrane by the time they reach  $r/a \sim 0.7$  (C).

D-F: The GLUT3 glucose transporter protein labels the cytoplasm of peripheral fibre cells (D) but this signal re-locates predominantly to the narrow sides of the cells by  $r/a \sim 0.8$  (E); later, at  $r/a \sim 0.7$ , GLUT3 signal is widely distributed around the rounded fibre cell membranes.

G-I: The membrane protein MP20 is distributed in a granular pattern resembling cytoplasmic vesicles, from the lens periphery to  $r/a \sim 0.7$  (G, H), where it is rapidly targeted to the plasma membrane (I). Scale bars: Top, 50  $\mu\text{m}$ ; A-C, D-F and G-I, 5  $\mu\text{m}$ .

confocal microscopy. These experiments revealed different patterns of cell-cell coupling at different radial locations. In peripheral fibre cells, where large broad side plaques predominate, dye diffusion occurred primarily in a radial direction (Figure 3B). In contrast, at locations beyond the zone of nuclear loss, where plaques were distributed more evenly around the fibre cell membrane, the pattern of fluorescein diffusion was approximately isotropic (Figure 3C). Thus the local pattern of intercellular coupling changed from a radial direction in the lens periphery to a

more uniform pattern in the deeper fibre cells, consistent with the differentiation-dependent remodeling of gap junction plaques. It appears, then, that the structure of gap junctions is modified by precise connexin processing and plaque remodeling, which create functional specializations in sub-regions of the organ and allow the maintenance of lens circulation, homeostasis and transparency.

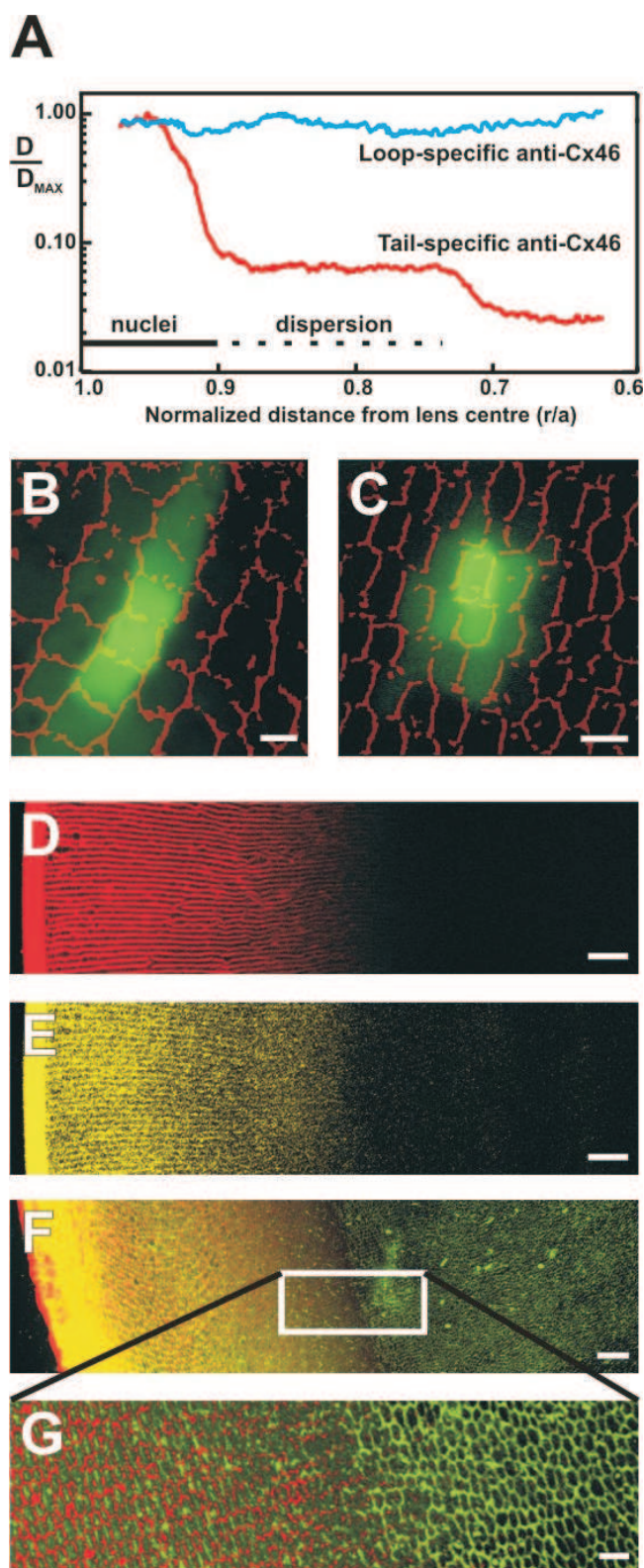


**Figure 3. Novel insights gained from an image-based approach to lens function.**

**A:** Precise in situ localization of two cleavage zones of Cx46, in relation to fibre cell differentiation markers. Two antibodies, specific to the cytoplasmic loop or the carboxy terminus ‘tail’ of Cx46, were used to label rat lens sections by immunofluorescence. Fluorescence signal density was imaged and quantified using a two-photon microscope and custom-written software. The density of membrane signal from the Cx46 tail antibody declined rapidly in two discrete zones located at  $r/a \sim 0.9$  and  $\sim 0.7$ , while the Cx46 loop antibody signal remained relatively constant, indicating cleavage of the carboxy tail in the two zones, with retention of the rest of the protein in the membrane. The solid and dotted horizontal lines designate the locations of axially clustered or dispersed fibre cell nuclei, respectively, preceding complete nuclear degradation.

**B, C:** Position-dependent patterns of local cell-cell coupling in the rat lens revealed by dye transfer. Two-photon flash photolysis was used to optically release caged fluorescein within individual fibre cells. Simultaneous confocal imaging of the time course of dye diffusion revealed that cell coupling was predominantly in a radial direction at the lens periphery (**B**) but was more isotropic deep in the lens ( $r/a < 0.7$ ; **C**). These patterns correlate with the sub-cellular distributions of gap junction channels in the respective areas.

**D, E:** Restricted dye diffusion into the lens. Cultured rat lenses were incubated for 4 hours in Texas Red-dextran (**D**) or Lucifer yellow (**E**), then fixed, sectioned and imaged. Both dyes penetrated the lens via the extracellular space to a depth of only  $\sim 400 \mu\text{m}$ , corresponding to the zone of nuclear degradation.

**F, G:** Antibodies to MP20 were applied to lens sections following dye treatment as in (**D**) for 18 hours. Immunofluorescent imaging of the sections showed that localization of MP20 to the cell membranes occurs at a depth corresponding to the limit of extracellular dye diffusion (**F**: red, Texas Red-dextran; green, MP20; **G**: high-magnification view), suggesting a possible role for MP20 in this ‘diffusion barrier’. Scale bars: **B, C**,  $5 \mu\text{m}$ ; **D-F**,  $50 \mu\text{m}$ ; **G**,  $10 \mu\text{m}$ .

*Glucose transporters: differential expression and membrane insertion*

Glucose is the principal fuel used by the lens to support growth and homeostasis<sup>23</sup>. In the lens, epithelial

and differentiating fibre cells are capable of oxidative phosphorylation, while the mature fibre cells, having lost their mitochondria, must rely solely on glycolysis for energy production<sup>2</sup>. The lens is bathed by the aqueous humor, which contains glucose levels that mirror those in

the plasma. Hence, lens cells near the periphery have access to an abundant supply of glucose, while the supply of glucose to the deeper-lying fibre cells is likely to be limited by a decreasing glucose gradient. However, the circulating current is thought to create a net flux of solutes that generates an extracellular fluid flow<sup>4,17</sup>, which in turn conveys nutrients toward the deeper-lying fibre cells by advection. Thus, from the model one might predict that both the peripheral and deeper-lying cells would be exposed to external glucose, though at different concentrations, and might express glucose transporters. To address this issue we performed a molecular profiling of GLUT isoform expression in the rat lens<sup>24</sup>. We found that epithelial cells express GLUT1 while cortical fibre cells express the higher-affinity GLUT3 isoform. This differential expression pattern is consistent with the probable glucose environments these cells are exposed to. In epithelial cells, the expression of GLUT1 appears to determine that the  $K_m$  of the glucose transporter is appropriate for the glucose concentration in the aqueous humor. In cortical fibre cells, the lower  $K_m$  of GLUT3 is likely to be more appropriate for extracting glucose from the extracellular fluid, which at this distance into the lens should have a relatively low glucose concentration.

Subsequent analysis of GLUT3 expression using our high-resolution image mapping approach revealed an intriguing pattern. Near the lens periphery, GLUT3 was located in the cytoplasm of fibre cells (Figure 2D); but with increasing depth into the lens, GLUT3 labeling became associated with the membrane, suggesting that GLUT3 undergoes a differentiation-dependent membrane insertion<sup>5</sup>. Interestingly, this membrane insertion of GLUT3 was initially targeted to the narrow sides of fibre cell membranes (Figure 2E). Then at a later stage of fibre cell differentiation, GLUT3 became more uniformly dispersed around the entire cell membrane (Figure 2F). The dispersal of GLUT3 from the narrow sides to the rest of the membrane appears to coincide with dispersal of the gap junction plaques which are initially located on the broad sides of fibre cells (Figure 2A-C). This observation reinforces our impression that the distinct sub-domains of fibre cell lateral membranes are lost during the course of differentiation. Our findings also suggest that GLUT3 is initially produced in the younger, peripheral fibre cells (which are capable of protein synthesis) and can be stored in the cytoplasm until a differentiation-dependent signal triggers its insertion into the membrane.

#### *Fibre cell adhesion: MP20 membrane insertion and extracellular diffusion*

Membrane insertion would appear to be a common phenomenon in the lens. High-resolution mapping of the distribution of the second most abundant lens membrane protein, MP20, revealed that like GLUT3 it undergoes a differentiation-dependent membrane insertion. Despite its relative abundance, the function of MP20 in the lens is still not definitively known. MP20 has been implicated as a component of membrane junctions between lens fibre

cells<sup>19,25</sup>, and more recently it was shown that MP20 acts as a ligand for galectin-3<sup>26</sup>, a known modulator of cell-cell adhesion in other tissues<sup>27</sup>. These results are consistent with a role for MP20 in cell-cell adhesion, however, the precise role of MP20 in lens structure, and its impact on lens function, have yet to be determined.

Using image-based immunofluorescent mapping, we assessed the relative distributions of MP20 and another abundant membrane protein, the water channel AQP0, as a function of fibre cell differentiation. We found that MP20, but not AQP0, is inserted into the fibre cell membranes at the stage when the cells lose their nuclei<sup>6</sup>. We showed that while MP20 labeling is intracellular in the younger fibre cells of the cortex, it redistributes to the plasma membranes as the cells mature (Figure 2G-I). Furthermore, the redistribution from the cytoplasm to the plasma membrane is relatively rapid and occurs over a small number of cell layers. If MP20 is indeed an adhesion molecule then the insertion of MP20 into the membranes of mature fibre cells might be expected to increase adhesion between the cells. This suggested to us the possibility that upon insertion of MP20, the extracellular space might become effectively smaller or more tortuous, restricting extracellular diffusion of molecules deeper into the lens. To test this hypothesis, we organ-cultured lenses in the presence of two fluorescent extracellular space markers, Texas Red-dextran (MW 10 kDa) and Lucifer yellow (MW 456 Da), for varying times. Regardless of the incubation period (2 to 18 hours), Texas Red-dextran diffusion into the lens only occurred up to a distance of some 400  $\mu\text{m}$  in from the capsule (Figure 3D). This consistency in the depth of tracer penetration observed at all time points indicated that the Texas Red-dextran movement via the extracellular space was not diffusion-limited, but restricted by a physical barrier. In support of this, the extracellular diffusion of the smaller molecular weight dye, Lucifer yellow, also became restricted at around the same depth (Figure 3E). This indicates that the barrier to extracellular diffusion has a molecular weight cut-off of at most  $\sim 450$  Da. Subsequent immunolabelling with MP20 antibodies of sections derived from a lens incubated in Texas Red-dextran for 18 hours indicated that the barrier to extracellular diffusion coincides with the zone where MP20 is inserted into the membrane (Figure 3F, G). Thus the insertion of MP20 correlates with the formation of a diffusion barrier that restricts the further extracellular movement of tracer dye molecules into the lens core. These results are consistent with the view that membrane insertion of MP20 contributes to the establishment of interactions between adjacent fibre cells, which act in the lens to limit the movement of molecules via the extracellular space.

#### **Conclusions and future challenges**

Our adoption of a functional imaging approach to investigate key components of the lens microcirculation system has reaped unforeseen insights into lens biology. It appears that the lens adopts a number of strategies to compensate for the inability of its older anucleate fibre cells to synthesise new membrane proteins. These strategies

involve the processing, redistribution and differential targeting of proteins as fibre cells age. The gap junction proteins Cx46 and Cx50 undergo specific, differentiation-dependent post-translational modifications that remove their cytoplasmic tails: events which cause a loss of junctional pH sensitivity and which bracket (temporally and spatially) a dramatic redistribution of gap junction plaques. This redistribution correlates with a major redirection of the local cell-cell coupling which underpins the lens microcirculation system. In a similar vein, the differentiation-dependent expression of glucose transporters, which targets the GLUT1 isoform to epithelial cells and the GLUT3 isoform to cortical cells, appears to match transporter affinity with local glucose availability. In order to achieve this, GLUT3 undergoes insertion into fibre cell narrow side membranes, apparently from a pre-designated cytoplasmic pool. Like GLUT3, MP20 also undergoes a membrane insertion event, but at a later stage of fibre cell differentiation, suggesting that the signals responsible for the insertion of these two membrane proteins are different. Insertion of MP20 correlates with the formation of an extracellular diffusion barrier. Taken together, our results show that as fibre cells mature and their ability to synthesise new membrane proteins is lost, the lens deploys a panoply of post-translational processing and targeting mechanisms to enable fibre cells to meet the physiological challenges associated with being buried ever deeper in the lens mass.

Since the lens is continually adding new fibre cells at its equator, it is interesting to speculate that establishing and maintaining spatial differences in membrane transport proteins is an integral part of the fibre cell differentiation programme. Having developed image-based methods to precisely map, with high resolution, spatial changes in membrane protein distribution, the next challenge is to identify the differentiation signals that trigger the very precise changes we have observed. If this is achieved, the lens will not only be an excellent model system in which to study generic aspects of cell differentiation but could also become a unique system in which to study how differentiation processes modulate overall tissue function.

#### Acknowledgements

Research work in the authors' laboratories was supported by: the Health Research Council of New Zealand, the Marsden Fund (NZ), the Wellcome Trust (UK), the Lotteries Grant Board (NZ), the University of Auckland Research Committee and the Auckland Medical Research Foundation.

#### References

- Menko AS. Lens epithelial cell differentiation. *Exp. Eye Res.* 2002; 75: 485-490.
- Bassnett S. Lens organelle degradation. *Exp. Eye Res.* 2002; 74: 1-6.
- Mathias RT, Rae JL, Baldo GJ. Physiological properties of the normal lens. *Phys. Rev.* 1997; 77: 21-50.
- Donaldson P, Kistler J, Mathias RT. Molecular solutions to mammalian lens transparency. *News Phys. Sci.* 2001; 16: 118-123.
- Merriman-Smith BR, Krushinsky A, Kistler J, Donaldson PJ. Expression patterns for glucose transporters GLUT1 and GLUT3 in the normal rat lens and in models of diabetic cataract. *Invest. Ophthalmol. Vis. Sci.* 2003; 44: 3458-3466.
- Grey AC, Jacobs MD, Gonen T, Kistler J, Donaldson PJ. Insertion of MP20 into lens fibre cell plasma membranes correlates with the formation of an extracellular diffusion barrier. *Exp. Eye Res.* 2003; 77: 567-574.
- Young MA, Tunstall MJ, Kistler J, Donaldson PJ. Blocking chloride channels in the rat lens: Localized changes in tissue hydration support the existence of a circulating chloride flux. *Invest. Ophthalmol. Vis. Sci.* 2000; 41: 3049-3055.
- Jacobs MD, Soeller C, Sisley AMG, Cannell MB, Donaldson P. Gap junction processing and redistribution revealed by quantitative optical measurements of connexin46 epitopes in the lens. *Invest. Ophthalmol. Vis. Sci.* 2004; 45: 191-199.
- Jacobs MD, Donaldson PJ, Cannell MB, Soeller C. Resolving morphology and antibody labeling over large distances in tissue sections. *Microsc. Res. Tech.* 2003; 62: 83-91.
- Bassnett S, Missey H, Vucemilo I. Molecular architecture of the lens fiber cell basal membrane complex. *J. Cell Sci.* 1999; 112: 2155-2165.
- Goodenough DA. The crystalline lens. A system networked by gap junctional intercellular communication. *Semin. Cell Biol.* 1992; 3: 49-58.
- Willecke K, Eiberger J, Degen J et al. Structural and functional diversity of connexin genes in the mouse and human genome. *J. Biol. Chem.* 2002; 277: 725-737.
- Paul DL, Ebihara L, Takemoto LJ, Swenson KI, Goodenough DA. Connexin46, a novel lens gap junction protein, induces voltage-gated currents in nonjunctional plasma membrane of *Xenopus* oocytes. *J. Cell Biol.* 1991; 115: 1077-1089.
- White TW, Bruzzone R, Goodenough DA, Paul DL. Mouse Cx50, a functional member of the connexin family of gap junction proteins, is the lens fiber protein, MP70. *Mol. Biol. Cell* 1992; 3: 711-720.
- Gao J, Sun X, Yatsula V, Wymore RS, Mathias RT. Isoform specific function and distribution of Na/K pumps in the frog lens epithelium. *J. Membr. Biol.* 2000; 178: 89-101.
- Gruijters WTM, Kistler J, Bullivant S. Formation, distribution and dissociation of intercellular junctions in the lens. *J. Cell. Sci.* 1987; 88: 351-359.
- Baldo GJ, Mathias RT. Spatial variations in membrane properties in the intact rat lens. *Biophys. J.* 1992; 63: 518-29.
- Gong XH, Baldo GJ, Kumar NM, Gilula NB, Mathias RT. Gap junctional coupling in lenses lacking alpha(3) connexin. *Proc. Nat. Acad. Sci.* 1998; 95: 15303-15308.

19. Tenbroek E, Arneson M, Jarvis L, Louis C. The distribution of the fiber cell intrinsic membrane proteins MP20 and connexin46 in the bovine lens. *J. Cell Sci.* 1992; 103: 245-57.
20. Kistler J, Bullivant S. Protein processing in lens intercellular junctions: cleavage of MP70 to MP38. *Invest. Ophthalmol. Vis. Sci.* 1987; 28: 1687-1692.
21. Lin JS, Fitzgerald S, Dong YM, Knight C, Donaldson P, Kistler J. Processing of the gap junction protein connexin50 in the ocular lens is accomplished by calpain. *Eur. J. Cell Biol.* 1997; 73: 141-149.
22. Lin JS, Eckert R, Kistler J, Donaldson P. Spatial differences in gap junction gating in the lens are a consequence of connexin cleavage. *Eur. J. Cell Biol.* 1998; 76: 246-250.
23. Berman ER. *Biochemistry of the Eye*. New York: Plenum Press, 1991.
24. Merriman-Smith R, Donaldson P, Kistler J. Differential expression of facilitative glucose transporters GLUT1 and GLUT3 in the lens. *Invest. Ophthalmol. Vis. Sci.* 1999; 40: 3224-3230.
25. Arneson ML, Louis CF. Structural Arrangement Of Lens Fiber Cell Plasma Membrane Protein Mp20. *Exp. Eye Res.* 1998; 66: 495-509.
26. Gonen T, Grey AC, Jacobs MD, Donaldson PJ, Kistler J. MP20, the second most abundant lens membrane protein and member of the tetraspanin superfamily, joins the list of ligands of galectin-3. *BMC Cell Biol.* 2001;17.
27. Perillo NL, Marcus ME, Baum LG. Galectins: versatile modulators of cell adhesion, cell proliferation, and cell death. *J. Mol. Med.* 1998; 76: 402-412.

---

Received 22 June 2004, in revised form 23 July 2004.

Accepted 24 July 2004.

©P.J. Donaldson 2004.

*Author for correspondence:*

Paul Donaldson  
Department of Physiology  
School of Medical Sciences  
University of Auckland  
Private Bag 92019  
Auckland, New Zealand

Phone: +64 9 3737599

Fax: +64 9 3737499

E-mail: p.donaldson@auckland.ac.nz



## Quantitative phase microscopy – a new tool for investigating the structure and function of unstained live cells

Claire L. Curl, Catherine J. Bellair\*, Peter J. Harris, Brendan E. Allman†,  
Ann Roberts\*, Keith A. Nugent\* & Lea M.D. Delbridge

*Department of Physiology and \*School of Physics, University of Melbourne, Victoria 3010, Australia  
and*

*†Imaging Division, IATIA Ltd., 2/935 Station St, Box Hill Nth, Victoria 3129, Australia*

### Summary

1. The optical transparency of unstained live cell specimens limits the extent to which information can be recovered from bright field microscopic images as these specimens generally lack visible, amplitude modulating components. However, visualization of the phase modulation which occurs when light traverses these specimens can provide additional information.

2. Optical phase microscopy, and derivatives of this technique such as Differential Interference Contrast (DIC) and Hoffman Modulation Contrast (HMC) have been widely used in the study of cellular materials. With these techniques enhanced contrast is achieved, which is useful in viewing specimens, but does not allow quantitative information to be extracted from the phase content available in the images.

3. An innovative computational approach to phase microscopy, which provides mathematically derived information about specimen phase modulating characteristics, has recently been described. Known as Quantitative Phase Microscopy (QPM), this method derives quantitative phase measurements from images captured using a bright-field microscope without phase or interference contrast optics.

4. The phase map generated from the bright field images by the QPM method can be used to emulate other contrast image modes (including DIC and HMC) for qualitative viewing. QPM achieves improved discrimination of cellular detail, which permits more rigorous image analysis procedures to be undertaken when compared with conventional optical methods.

5. The phase map contains information about cell thickness and refractive index and can allow quantitation of cellular morphology under experimental conditions. As an example, the proliferative properties of smooth muscle cells have been evaluated using QPM to track growth and confluency of cell cultures. QPM has also been used to investigate erythrocyte cell volume and morphology in different osmotic environments.

6. QPM is a valuable new non-destructive, non-interventional experimental tool for structural and functional cellular investigations.

### Introduction

One of the major difficulties in visualizing and imaging cellular material is the lack of contrast inherent in

these translucent specimens. With fixed specimens contrast may be created using staining techniques, but for work with live cells this is usually not possible. To facilitate the visualization of viable cellular specimens, a number of different forms of phase microscopy have been devised where contrast is enhanced by manipulation of the optical path. In this review the principles underlying these methods of optical phase microscopy and the limitations associated with their implementation are discussed. A recently developed new form of phase microscopy, Quantitative Phase Microscopy (QPM), is described. The utility of QPM, which incorporates qualitative aspects of established phase techniques and also offers the capacity to undertake quantitative structural analysis, is evaluated. Finally some applications of the QPM methodology are briefly presented.

### *Light Propagation and Phase Properties of Cellular Material*

When light waves traverse a stained sample some light is absorbed by the localised pigment. Thus the amplitude of the light waves emergent from specific regions of the specimen are altered relative to the background or medium.<sup>1</sup> This modulation allows visualisation by the human eye, and sensitivity to differences in amplitude are perceived as variation in brightness and colour. When light traverses an unstained sample there is little change in the amplitude of the light since the unpigmented sample does not have substantial absorption properties in the visible wavelengths usually employed for microscopy. A lack of amplitude modulating structure renders the sample translucent and morphology difficult to discern. However, light propagated through a translucent sample is altered so that the phase is displaced with respect to the light which has passed through the surrounding medium only. Such a displacement is termed phase retardation or phase shift.<sup>2</sup>

The 'phase shift effect' produced by a sample simply reflects the extent to which light wave propagation is slowed down by passage through the sample. Waves passing through a thick sample will be slowed to a greater degree than those passing through a thin sample. This effect is illustrated in Figure 1. Incident light waves are initially 'in phase', and as sample regions of different thickness and different composition (relative to the medium) influence the passage of the light, a variable degree of phase retardation is induced. The extent to which the emergent light waves are 'out of phase' with each other is termed the relative

phase shift and is measured in radians.<sup>2,3</sup> Unlike amplitude variations, differences in phase cannot be perceived by the eye or by photographic film.

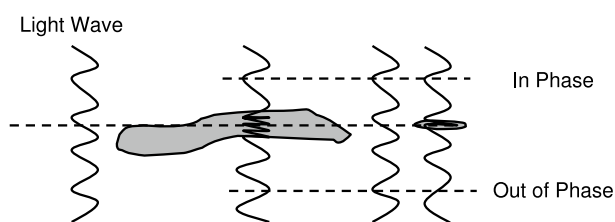


**Figure 1. Schematic representation of the phase retardation of light as it passes through a sample.**

Light waves are 'in phase' before passing through the specimen, but are 'out of phase' emerging from cell regions of non-uniform thickness due to the effects of phase retardation.

### Optical Phase Microscopy

The optical phase microscope was developed to allow visualisation of the phase properties of unstained cellular material and works by converting phase properties to amplitude differences that can be detected by eye. Different forms of optical phase microscopy utilise various optical devices that change the way light is refracted and reflected and these have served for many years as useful tools for qualitative examination of unstained live cells. An overview of the major types of phase microscopy is provided below, and the advantages and disadvantages of each are briefly considered.

#### Zernike Phase Microscopy

The 'standard' (Zernike) phase microscope, invented in the 1930's by the Dutch physicist Fritz Zernike,<sup>4</sup> uses a phase plate to alter the passage of light passing directly through a sample by a specified wavelength fraction. This method results in destructive interference of light and allows details of the normally transparent cellular specimen to appear relatively dark against a light background. That is, the phase differences are converted into amplitude differences and observed as intensity contrast. The extent of phase shift induced is determined by a combination of the refractive index and thickness of a specimen at any point.<sup>5</sup> By this means, structures of unstained living cells, not evident using bright field microscopy, can be visualised using optical phase microscopy. A major disadvantage of Zernike phase microscopy is the appearance of light halos at the edges of specimen components where the phase shift gradient is most steep, resulting in poor boundary localisation. These boundary halo effects are particularly problematic if quantification of cell size and/or structure is required.<sup>1,6-8</sup>

#### Differential Interference Contrast (DIC)

Differential interference contrast microscopy was invented in the 1950's by the French optics theoretician, George Nomarski.<sup>9</sup> DIC is based on modification of the Wollaston prism which is used for detecting optical gradients in specimens and converting them into intensity differences.<sup>2</sup> The equipment needed for DIC microscopy includes a polarizer, a beam-splitting modified Wollaston prism below the condenser, another prism above the objective, and an analyzer above the upper prism.<sup>10</sup> The prisms allow for splitting of the incident light in the optical path before reaching the specimen and re-combination of the split beams beyond the specimen. As a result the paths of the parallel beams are of unequal length and when re-combined allow differences in intensity to be discerned.<sup>11</sup> Under DIC conditions one side of the specimen appears bright while the other side appears dark, conferring a three-dimensional 'shadow relief' appearance.<sup>8</sup> An aesthetic colour effect may also be achieved with DIC when there is a further phase shift produced by a wave plate inserted in the light path. A major advantage of DIC is that it makes full use of the numerical aperture of the system and permits focus in a thin plane section of a thick specimen, with reduced contributions from specimen regions above or below the plane of focus. Thus DIC provides superior resolution to Zernike phase contrast microscopy<sup>10</sup> and when coupled with other equipment allows optical sectioning.<sup>12</sup> DIC has the additional advantage that the 'halo' edge effects produced by standard phase microscopy are largely absent.<sup>10</sup> Unfortunately DIC is expensive to set up due to the cost of the accessory optical components, requires significant increases in incident light levels and is not conducive to imaging with plastic culture dishes (which mix the phase retardation effects with birefringence). Implementation of DIC can also be physically restrictive, as the condenser position over the stage of an inverted microscope can obstruct access for placement of experimental tools (ie recording electrodes, solution spritzers).

#### Hoffman Modulation Contrast (HMC)

Hoffman Modulation Contrast, invented by Robert Hoffman in 1975,<sup>13,14</sup> is similar to DIC, but works by the conversion of optical gradients into variations in light intensity.<sup>15,8</sup> The components of the HMC system comprise an amplitude spatial filter (the 'modulator') placed at the back focal plane of an objective, and an off-centre slit partially covered by a polarizer located at the front plane of the condenser. Hoffman images have a three-dimensional appearance arising from the directional effect of the optical gradients. Like DIC, a major advantage of HMC is that fuller use of the numerical aperture results in excellent resolution of detail together with good specimen contrast and visibility. HMC can be used for imaging through plastic culture ware, and it is for this application that the technique is most widely utilised. Although the Hoffman 'view' takes on a three-dimensional appearance, localisation of image detail at a particular depth within the sample is relatively

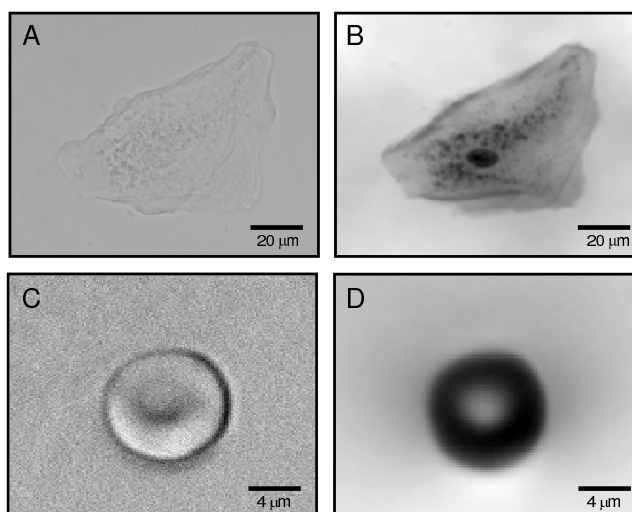


**Figure 2. Example of the ability of QPM to highlight cellular morphology by creating of phase maps.**

All bright field images presented in Figures were acquired using a black and white 1300 × 1030 pixel Coolsnap FX CCD camera (Roper Scientific) mounted on a Zeiss Axiovert 100M inverted microscope. The defocus images were obtained using a piezoelectric positioning device (PiFoc, Physik Instrumente, Karlsruhe, Germany) for objective translation. Bright field images were processed to generate phase maps using QPm software (v2.0 IATIA Ltd, Australia).

**A:** Bright field image of human buccal epithelial cell (Achromplan, ×40, NA 0.60).

**B:** Phase map of cell shown in A, showing prominent phase-dense (darker) nucleus.

**C:** Bright field image of mouse erythrocyte (Achromplan, ×63, NA 0.80).

**D:** Phase map of erythrocyte shown in C, with biconcavity depicted as a darkened annulus of increased phase.

imprecise<sup>1</sup> and this can make spatial navigation through a specimen visually difficult. As with DIC, HMC also involves a number of ancillary optical components and is relatively expensive to implement.

### **Quantitative Phase Microscopy**

It is important to emphasise that the optical microscopy techniques discussed above, whilst very useful in many different observational and imaging situations, generally only provide qualitative information about cellular morphology.<sup>7</sup> An innovative computational approach to phase microscopy, which provides mathematically derived information about specimen phase modulating characteristics, has recently been described.<sup>16,17</sup> Known as Quantitative Phase Microscopy (QPM), this method combines the useful qualitative attributes of previous phase imaging approaches with the additional advantage of quantitative representation of specimen phase parameters. With QPM, a phase-based analysis of cell structure, morphology and composition is possible using a relatively simple wide field microscope. In optical phase microscopy the amplitude and phase image components are inextricably embedded in the image generated, whereas with QPM it is possible to separate these specimen qualities in the images produced.

The implementation of QPM involves the calculation of a 'phase map' from a triplicate set of images captured under standard bright field microscopy.<sup>5</sup> A computational algorithm is applied to the analysis of an in-focus image and a pair of equidistant positive and negative de-focus

images. The mathematical processes involved have been described in detail elsewhere, but essentially the procedure entails calculation of the rate of change of light intensity between the three images in order to determine the phase shift induced by the specimen.<sup>5</sup> The de-focus images may be obtained either by positioning a mirror at specified points in the optical path or by translating the objective to positions above and below the designated plane of focus. Both the image acquisition and the computational processes for QPM can be directed by commercially available hardware and software (QPm software, IATIA Ltd, Box Hill Nth, Australia).

### **Using QPM for Qualitative Evaluation of Cell Morphology**

QPM is particularly valuable for examining cellular morphology, especially when visualising phase dense components of cellular structures such as the nucleus, organelles or intracellular inclusions. Figure 2A shows an example of a typical bright field image of a buccal epithelial cell, from which little evidence of detailed intracellular structure can be gleaned. When a phase map is generated from bright field images using QPM methods (Figure 2B), the phase information within the cell becomes apparent with visualisation of the intracellular organelles, including the very obvious phase dense (dark) nucleus. As a further example, Figure 2C shows a bright field image of an erythrocyte exhibiting a characteristic biconcave disk-like shape. The calculation of the phase map using QPM (Figure 2D) allows more detailed representation of the cell

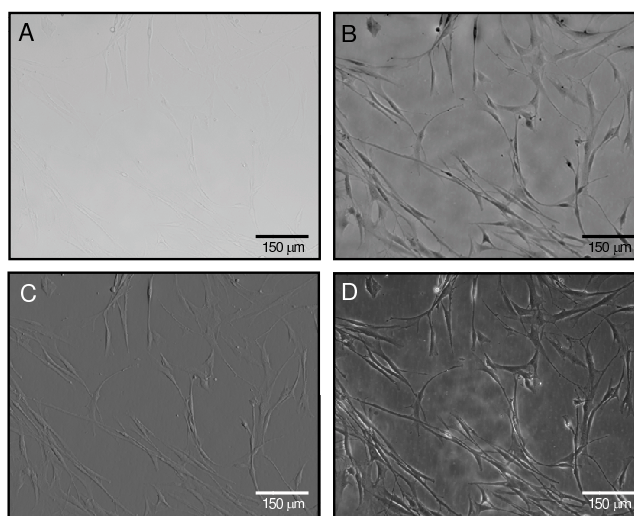


**Figure 3. Illustration of the different simulated imaging modalities generated using QPM applied to smooth muscle cells in culture (Achromplan  $\times 10$ , NA 0.30).**

**A:** Bright field image of human airway smooth muscle cells.

**B:** Phase map produced using bright field image in Panel A.

**C:** Differential Interference Contrast (DIC) image calculated from phase map.

**D:** Hoffman Modulation Contrast (HMC) image calculated from phase map.

geometry, with the biconcavity appearing as a well defined annulus of increased cell 'phase' thickness.

The phase information which is extracted from wide field cell imaging by QPM analysis may also be utilized to simulate optical phase and to reproduce different imaging modalities. For example in Figure 3A, a bright field image of a smooth muscle cell culture is shown, notable for the lack of contrast and definition. In Figure 3B the phase map calculated from the triplicate set of bright field images of the same cell field exhibits considerably enhanced contrast and cellular delineation. Based on the information within the phase map, mathematical procedures can be applied to allow calculation and creation of images usually associated with optical imaging modalities such as DIC (Figure 3C), Hoffman Modulation Contrast (Figure 3D), Zernike Phase Contrast and Dark Field. This is a useful and efficient extension of the QPM analysis approach, as these different image modes are all derived from the same initial bright field image set without any specialized optical equipment. Compared with other techniques, QPM is optically and practically simple, requiring only a bright field microscope and a CCD camera to generate a range of imaging modalities. An additional convenience is that with QPM, the bright field imaging conditions do not require that a condenser be positioned close above the inverted microscope stage, and this allows for improved access of other equipment such as electrodes and pipettes.

#### **Using QPM for Quantitative Assessment of Cellular Morphology**

The use of QPM for quantitative assessment of cell attributes has considerable potential, and a number of such

applications have already been developed.<sup>18,19</sup> These include the tracking of culture confluency and growth<sup>20</sup> to investigate cell proliferative properties, and the development of cell volume measurement techniques<sup>21</sup> to evaluate variations in erythrocyte morphology.

#### **Tracking Cell Culture Confluency and Growth**

The relatively high degree of contrast which is achieved in phase maps generated by QPM analysis make these images especially amenable to segmentation and thresholding manipulations. This feature of QPM has been exploited to develop new tools for the quantitative evaluation of cell growth in culture, using repeated imaging of cultures to assess the progression towards confluency over designated periods of time.<sup>20</sup> It is important to appreciate that methodologies previously established for the measurement of cell growth in culture are either destructive or extremely laborious. These include cell size measurement with fluorescence activated cell sorting (FACS, which requires removal of cells from their substrate by trypsinization), cell protein synthesis estimation (using tritiated leucine uptake) or manual cell counting by haemocytometry.<sup>22-25</sup> The ability of QPM to provide quantitative information regarding the growth of cells *in situ* in culture provides a significant advance on these techniques.

The first step in the processing of QPM-derived phase maps to quantify the amount of cellular material involves the generation of a pixel intensity histogram to differentiate the phase values associated with cellular and non-cellular regions of the culture dish. From this histogram a threshold grey level is obtained at which segmentation of cellular from non-cellular material can be achieved to produce a

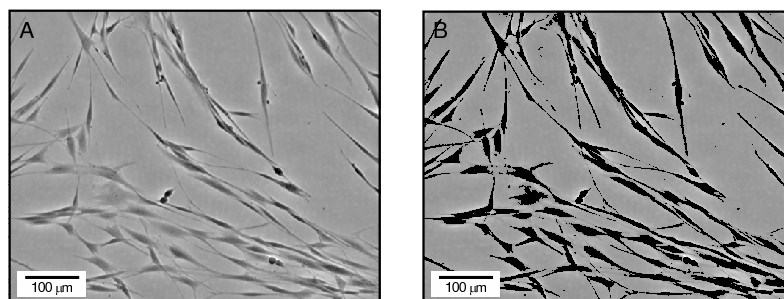


**Figure 4. Demonstration of the segmentation process used for assessing confluency of human airway smooth muscle cell cultures (*Achroplan*  $\times 10$ , NA 0.3).**

**A:** Phase map of human airway smooth muscle cell culture.

**B:** Segmented image of phase map in A, generated using the threshold value determined by axis intercept. (Image-Pro Plus software v3.0 Media Cybernetics, USA) See text for method details.

binary image (for a more detailed explanation of curve fitting and extrapolation procedures see Curl *et al* 2004<sup>20</sup>). This image manipulation process is illustrated in Figure 4 which shows a smooth muscle cell culture phase map (Figure 4A) calculated from a bright field image, and the segmented cell-delineated image produced by this thresholding process (Figure 4B). The area summation of the segmented cellular material on the culture plate provides a measure of the confluency of the cell culture, expressed as a percentage of the total field area examined (in this example calculated to be 17.05% of total field). The precision of this measurement relies on the threshold grey level extrapolated by curve-fitting methods applied to the image pixel intensity histogram<sup>20</sup> and is entirely reproducible for a given image. The extent to which histogram distributions vary from image to image will determine the measurement variability, and this should be evaluated empirically for different imaging conditions. As this methodology does not require the cells to be manipulated in any fashion (ie by staining or trypsinization), repeated measurements of the same cell field may be made over a specified time period to derive a growth curve. The high contrast phase visualization produced by the QPM technique makes these measurements feasible – the contrast available in bright field and even in conventional optical phase images is generally not adequate to permit reproducible image thresholding and reliable cell delineation.

#### Cellular Volume Measurement

Cell volume regulation is a fundamental cellular homeostatic mechanism.<sup>26</sup> Accurate measurements of cell volume can provide important information about many physiological regulatory and growth processes, but such measurements are particularly difficult to undertake *in situ*.<sup>12,27</sup>

As the extent of phase shift induced when light passes through a translucent cellular specimen is determined by a combination of the refractive index and thickness of the cell, it follows that, where refractive index

may be established (or is known already) it is also possible to use QPM to measure the thickness of a cell. Thus, the volume of an individual cell or of a field of cells may be measured by the integration of thickness values extracted from designated areas of the phase map. Erythrocytes, which adopt predictable and well characterized geometric shapes in different osmotic environments,<sup>28-31</sup> are a particularly convenient cell type for the demonstration of this application of QPM.<sup>21</sup>

When exposed to a sufficiently hypotonic solution, erythrocytes expand their isotonic biconcavity and take on spherical shape. In this condition, the red blood cell thickness (depth) may be equated with the width (measured in the x-y plane). From a specific cell a certain phase value can be correlated with the measured thickness/width. By averaging over many cells, a 'generic' erythrocyte refractive index can be determined.<sup>21</sup> This refractive index can then be applied to any similar cell, or fields of cells under equivalent circumstances to convert the phase values contained in the phase map (such as that shown in Figure 2D) to an estimate of cellular volume. Erythrocyte volume calculations performed using this methodology compare favourably with those previously reported using more laborious and destructive methods.<sup>32,33</sup> For other cell types with less convenient geometry, essentially the same process can be used to undertake volume measurement, although somewhat more complex procedures (ie confocal microscopy combined with QPM<sup>34</sup>) may be required to initially establish a value for refractive index when this is not independently available. As phase shift is simply the product of specimen thickness and refractive index, any error in the determination of the refractive index will be linearly reflected in the calculated volume. A refractive index of 1.59-1.63 is commonly reported for erythrocytes,<sup>35</sup> and taking values at either extreme of this range would produce about a 2.5% variation in computed volume. In most applications, where the refractive index is not expected to alter under experimental circumstances for a given cell type, phase changes can be taken to be directly proportional to changes in cell thickness (and therefore volume) for relative measurements.

As a newly devised microscopy technique, QPM has demonstrated application in the evaluation of cellular structure and morphology. The full value of QPM as a non-destructive, non-interventional experimental tool for functional imaging of 'real time' cellular process will become evident as this technique is more widely implemented.

#### Acknowledgements

The authors thank Mr David Stewart of Zeiss Australia for assistance with optical and software components and Assoc Prof. Alastair Stewart and Ms Trudi Harris (Department of Pharmacology, University of Melbourne) for generous assistance with cell culture preparation. The support of the Australian Research Council and IATIA Ltd is acknowledged. The quantitative phase microscopy system described is marketed by IATIA Ltd ('QPm', [www.iatia.com.au](http://www.iatia.com.au)) and we declare that KAN has a financial interest in that company.

#### References

1. DiBona DR, Kirk KL, Johnson RD. Microscopic investigation of structure and function in living epithelial tissues. *FASEB Fed. Proc.* 1985; **44**:2693-2703.
2. Ross KFA. Phase contrast and interference microscopy for cell biologists. Edward Arnold (Publishers) Ltd, London 1967.
3. McMahon PJ, Barone-Nugent ED, Allman BE, Nugent KA. Quantitative phase-amplitude microscopy II: differential interference contrast imaging for biological TEM. *J. Microsc.* 2002; **206**:204-208.
4. Zernike F. Phase contrast, a new method for the microscopic observation of transparent objects. *Physica* 1942; **9**:686-693.
5. Barty A, Nugent KA, Roberts A, Paganin D. Quantitative phase microscopy. *Opt. Lett.* 1998; **23**:817-819.
6. Delbridge LMD, Kabbara AA, Bellair CJ, Allman BE, Nassis L, Roberts A, Nugent KA. Quantitative phase imaging – a new way to 'see' cells. *Today's Life Science.* 2002; **14**:28-32.
7. Barer R. Refractometry and interferometry of living cells. *J. Opt. Soc. Am.* 1957; **47**:545-556.
8. Simon I, Pound CR, Partin AW, Clemens JQ, Christens-Barry WA. Automated image analysis system for detecting boundaries of live prostate cancer cells. *Cytometry.* 1998; **31**:287-294.
9. Nomarski G & Weill AR. Application a la metallographie des methods interferentielles a deux ondes polarises. *Rev. Metall.* 1955; **2**:121-128.
10. Salmon ED, Tran P. High-resolution video-enhanced differential interference contrast (VE-DIC) light microscopy. *Meth. Cell Biol.* 1998; **56**:153-184.
11. Allen RD, David GB, Nomarski G. The Zeiss-Nomarski differential interference equipment for transmitted-light microscopy. *Z. Wiss Mikrosk. Tech.* 1969; **69**:193-221.
12. Kimelberg HK, O'Connor ER, Sankar P, Keese C. Methods for determination of cell volume in tissue culture. *Can. J. Physiol. Pharmacol.* 1991; **70**:S323-S333.
13. Hoffman R & Gross L. The modulation contrast microscope. *Nature.* 1975; **254**:586-588.
14. Hoffman R, Gross L. Modulation contrast microscopy. *Appl. Optics.* 1975; **14**:1169-1171.
15. [www.micro.magnet.fsu.edu/primer/techniques/hoffman/hoffmanintro.html](http://www.micro.magnet.fsu.edu/primer/techniques/hoffman/hoffmanintro.html)
16. Paganin D & Nugent KA. Non-interferometric phase imaging with partially coherent light. *Phys. Rev. Lett.* 1998; **80**:2586-2589.
17. Barone-Nugent ED, Barty A, Nugent KA. Quantitative phase-amplitude microscopy I: optical microscopy. *J. Microsc.* 2002; **206**:194-203.
18. Allman BE, Nassis L, von Bibra ML, Bellair CJ, Kabbara AA, Barone-Nugent E, Gaeth AP, Delbridge LMD, Nugent KA. Optical phase microscopy: quantitative imaging and conventional phase analogs. *Microsc. Analy.* 2002; **52**:13-15.
19. Bellair CJ, Curl CL, Allman BE, Harris PJ, Roberts A, Delbridge LMD, Nugent KA. Quantitative phase-amplitude microscopy IV: imaging thick specimens. *J. Microsc.* 2004; **214**:62-70.
20. Curl CL, Harris T, Harris PJ, Allman BE, Stewart AG, Delbridge LMD. Quantitative phase microscopy: a new tool for measurement of cell culture growth and confluency in situ. *Pflugers Archiv.* 2004; **448**:462-468.
21. Curl CL, Bellair CJ, Allman BE, Roberts A, Nugent KA, Harris PJ, Delbridge LMD. Measurement of erythrocyte volume changes in response to osmotic stimuli using quantitative phase microscopy. *Proc. Exp. Biol.* 2003: LB65.
22. Fernandes DJ, Guida E, Kalafatis V, Harris T, Wilson J, Stewart AG. Glucocorticoids inhibit proliferation, cyclin D1 expression and retinoblastoma protein phosphorylation, but not mitogen-activated protein kinase activity in human cultured airway smooth muscle. *Am. J. Resp. Cell. Mol. Biol.* 1999; **21**:77-88.
23. Lepore DA, Hurley JV, Stewart AG, Morrison WA, Anderson RL. Prior heat stress improves the survival of ischemic-reperfused skeletal muscle in vivo: role of HSP 70. *Muscle Nerve.* 2000; **23**:1847-55.
24. Ravenhall CR, Guida E, Harris T, Koutsoubos V, Vadiceolo P, Stewart AG. The importance of ERK activity in the regulation of cyclin D1 levels in DNA synthesis in human cultured airway smooth muscle. *Br. J. Pharmacol.* 2000; **131**:17-28.
25. Stewart AG. Airway wall remodelling and hyper-responsiveness: modelling remodelling in vitro and in vivo. *Pulm. Pharmacol. Ther.* 2001; **14**:255-265.
26. Korchev YE, Gorelik J, Lab MJ, Sviderskaya EV, Johnston CL, Coombes CR, Vodyanoy I, Edwards CRW. Cell volume measurement using scanning ion conductance microscopy. *Biophys. J.* 2000; **78**:451-457.

27. Reuss L. Changes in cell volume measured with an electrophysiologic technique. *Proc. Natl. Acad. Sci.* 1985; **82**:6014-6018.
28. Orlov SN, Pokudin NI, Kotelevtsev YV, Gulak PV. Volume-dependent regulation of ion transport and membrane phosphorylation in human and rat erythrocytes. *J. Membr. Biol.* 1989; **107**:105-117.
29. MacKnight ADC, Gordon LGM, Purves RD. Problems in the understanding of cell volume regulation. *J. Exp. Zool.* 1994; **268**:80-89.
30. Schneider AS, Harmatz D. An experimental method correcting for absorption flattening and scattering in suspensions of absorbing particles: circular dichroism and absorption spectra of hemoglobin in situ in red blood cells. *Biochemistry.* 1976; **15**:4158-4162.
31. Gitter-Amir A, Rosenheck K, Schneider AS. Angular scattering analysis of the circular dichroism of biological cells. 1. The red blood cell membrane. *Biochemistry.* 1976; **15**:3131-3137.
32. Ponder E: Hemolysis and related phenomena, Grune & Statton, New York, 1948.
33. Altman PL, Dittmer DS: *Biology Data Book*, Federation of American Societies of Experimental Biology, Washington DC, 1964.
34. [www.iatia.com.au/applications/apps\\_confocal.asp](http://www.iatia.com.au/applications/apps_confocal.asp)
35. Mazarevica G, Freivalds T, Jurka A. Properties of erythrocyte light refraction in diabetic patients. *J. Biomed. Optics* 2002; **7**:244-247.

---

Received 7 July 2004, in revised form 27 July 2004.

Accepted 12 August 2004.

©L.M.D. Delbridge 2004.

Author for correspondence:

Lea Delbridge

Department of Physiology

University of Melbourne

Victoria, 3010

Australia

Tel: +61 3 8344 5853

Fax: +61 3 8344 5897

E-mail: [imd@unimelb.edu.au](mailto:imd@unimelb.edu.au)



## Microscopic imaging of extended tissue volumes

Ian LeGrice, Greg Sands, Darren Hooks, Dane Gerneke & Bruce Smaill

*Bioengineering Institute & Department of Physiology, University of Auckland, New Zealand*

### Summary

1. Detailed information about 3D structure is key to understanding biological function

2. Confocal laser microscopy has made it possible to reconstruct 3D organization with exquisite resolution at cellular and subcellular levels

3. There have been few attempts to acquire large image volumes using the confocal laser scanning microscope.

4. We have previously used manual techniques to construct extended volumes (several mm in extent, at 1.5  $\mu\text{m}$  voxel size) of myocardial tissue.

5. We are now developing equipment and efficient automated methods for acquiring extended morphometric databases using confocal laser scanning microscopy.

### Introduction

The association between form and function is a central principle of the biological sciences and one that has contributed to the growth of the field over many years. The linkage is probably more important today than ever before. It is widely accepted that detailed information about three-dimensional (3D) structure is key to understanding biological function from molecule to organ and with the development of new imaging modalities there has been an explosion in the quality and volume of data that can be acquired at each of these scales. For instance, the confocal laser microscope has made it possible to reconstruct three-dimensional organization with exquisite resolution at cellular and subcellular levels. Moreover, using the array of immuno-histochemical techniques now available, it is also possible to probe the link between structure and function directly, for instance by quantifying the co-location of labelled proteins such as gap junctions or receptors with other anatomic structures.

For the most part, confocal imaging has not been used to reconstruct 3D tissue organization in a systematic fashion and there have been few attempts to acquire large image volumes as has been done with MRI or micro-CT. This reflects the physical constraints on the technology. Acquisition rates are limited by the sensitivity of photodetectors and the need to scan points sequentially throughout the tissue volume, while the dimensions that can be imaged are set by the working field of the microscope objective and critically, with respect to Z direction, by absorption and scattering of light in the tissue investigated. That said, there is a clear need for databases that incorporate structural information across the scales addressed by confocal microscopy for normal and

pathologically changed organ systems at different developmental stages. Extended morphometric databases of this kind are required to characterize more fully the structural changes associated with various dysfunctional states and to support the computer models that are increasingly being used to integrate experimental information at cell, tissue and organ levels.

### Manual technique for acquiring extended confocal microscope images of biological samples

In the remainder of this section, we summarize ongoing research at the University of Auckland which is directed toward the development of efficient methods for acquiring extended morphometric databases using confocal laser microscopy. The work flows from initial studies in which high-resolution volume images were assembled of myocyte arrangement and connective tissue organization across the heart wall<sup>1</sup>. Transmural segments (800  $\mu\text{m}$   $\times$  800  $\mu\text{m}$   $\times$  4.5 mm) were cut from the left ventricle free wall of rat hearts, previously perfused with Bouin's solution for fixation and then with the dye picosirius red which binds non-sterically to collagen<sup>2</sup>. The specimen was dehydrated with a graded series of alcohols, embedded in epoxy resin and the upper surface of the block was then planed flat using an ultramicrotome. A motorized stage was used to control the horizontal position of the specimen and contiguous z-series image stacks were acquired at different x-y locations. In this way, an extended volume image was generated over the upper surface of the transmural specimen to a depth of around 60  $\mu\text{m}$ . The block was then removed from the microscope and mounted in an ultramicrotome where the upper 50  $\mu\text{m}$  was removed. The specimen was then returned to the microscope and the cycle of imaging and trimming was completed sequentially until the complete volume was imaged. Painstaking alignment of the upper surface of the tissue block in both the microtome and the confocal microscope was required at each stage in this process to ensure that image registration was, as far as possible, preserved (See Figures 1 and 2). Moreover, further *post-hoc* spatial transformation of image sub-volumes was still required to optimize registration when assembling the complete image volume.

Digital reslicing, segmentation and volume rendering methods can be applied to the resulting volumes to provide quantitative structural data about the 3D organization of myocytes, extracellular collagen matrix and the vascular network. These data have not previously been available and provide a powerful basis for further analysis of function. For example, it is a relatively trivial matter to quantify the transmural variation of perimysial collagen once it has been

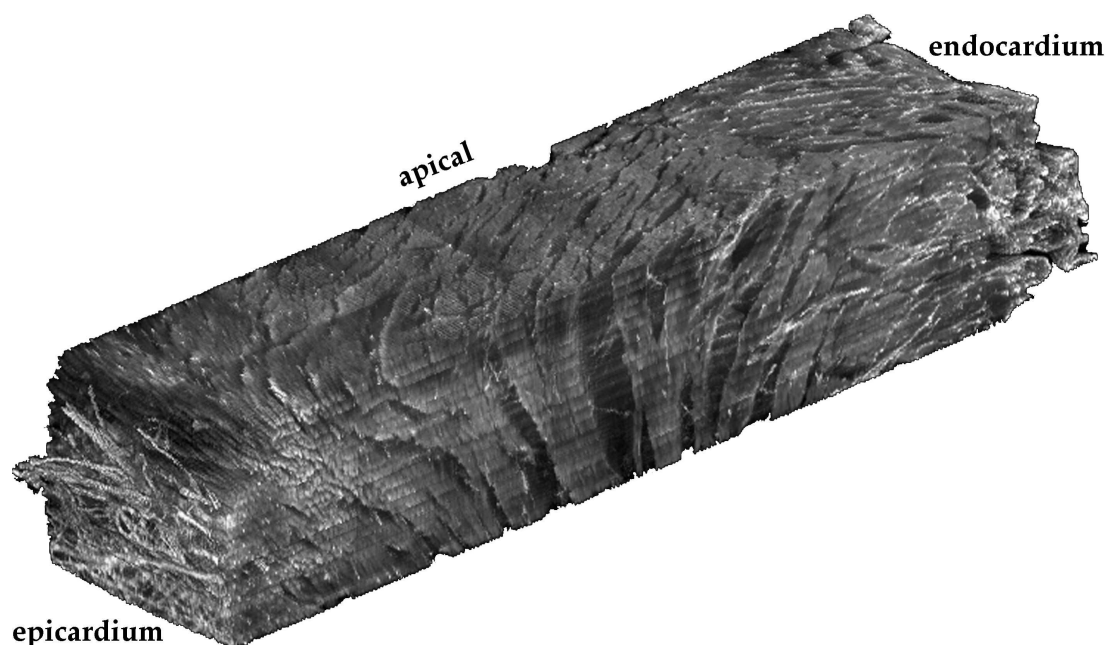


**Figure 1.** Oblique view of extended volume image from left ventricle of rat heart obtained using confocal microscopy. Note the laminar organization and collagen (white) interconnecting layers of myocytes. The epicardial collagen weave is clearly seen along with cleavage planes between myocardial layers. (From 1, with permission from the Royal Microscopical Society).

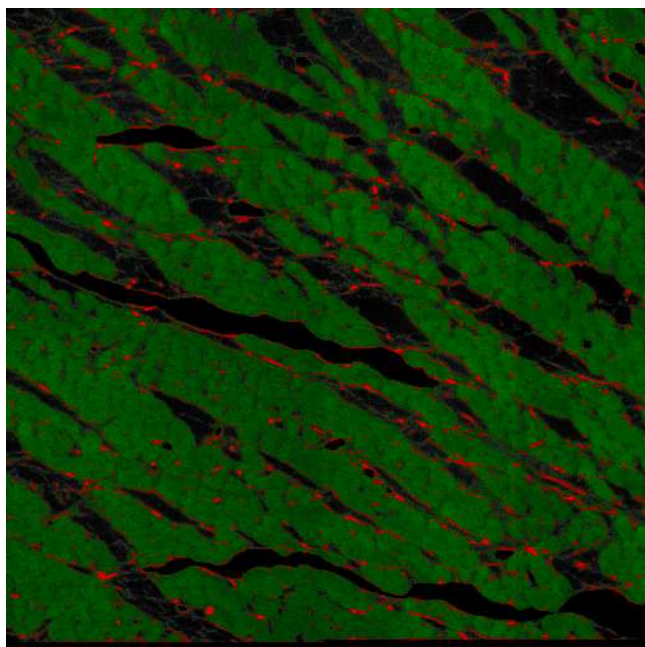


**Figure 2.** Image slice from left ventricular midwall of rat heart ( $800 \times 800 \mu\text{m}$ ) illustrating laminar organization of myocytes. Plane of optical section is perpendicular to myocyte axis. Red dots are perimysial collagen cords running parallel to myocyte axis.

segmented out of an extended volume image as shown in Figure 3b. The heart wall remodelling associated with many types of cardiac disease involves changes in the extent and

distribution of collagen and detailed information about the time-course of these changes is necessary to better understand the disease processes involved. It follows that extended volume imaging provides a pathway for systematic acquisition of such data. It can also be used for the development of computer models, which make it possible to examine the effects of myocardial structure on the function of the heart. For instance, we have extracted the 3D arrangement of cleavage planes and myocyte orientation from an extended volume image of rat left ventricular myocardium ( $3.8\text{mm} \times 0.8\text{mm} \times 0.8\text{mm}$  at  $1.5\mu\text{m}$  pixel size,  $0.72 \times 10^9$  voxels).

This application illustrates well the utility of being able to gather detailed microscopic information over extended volumes. The myocardial layers and cleavage planes are defined by connective tissue and myocytes interconnections that are visible at levels of a few micrometers and it is details of these structures that are needed to define the local electrical and mechanical properties of the laminar myocardium. However, the cleavage planes can extend for two to three millimetres. In order to fully describe the structure and associated material properties, for instance when developing a computer model of myocardium it is necessary to have information across a wide scale range, the system we have developed provides the tools to acquire this information. The extended volume image of rat myocardium has been incorporated into a structurally detailed, finite element model of ventricular myocardium that has been used to study the influence of discontinuous myocyte organization on the propagation of electrical activation in the heart<sup>3</sup>.

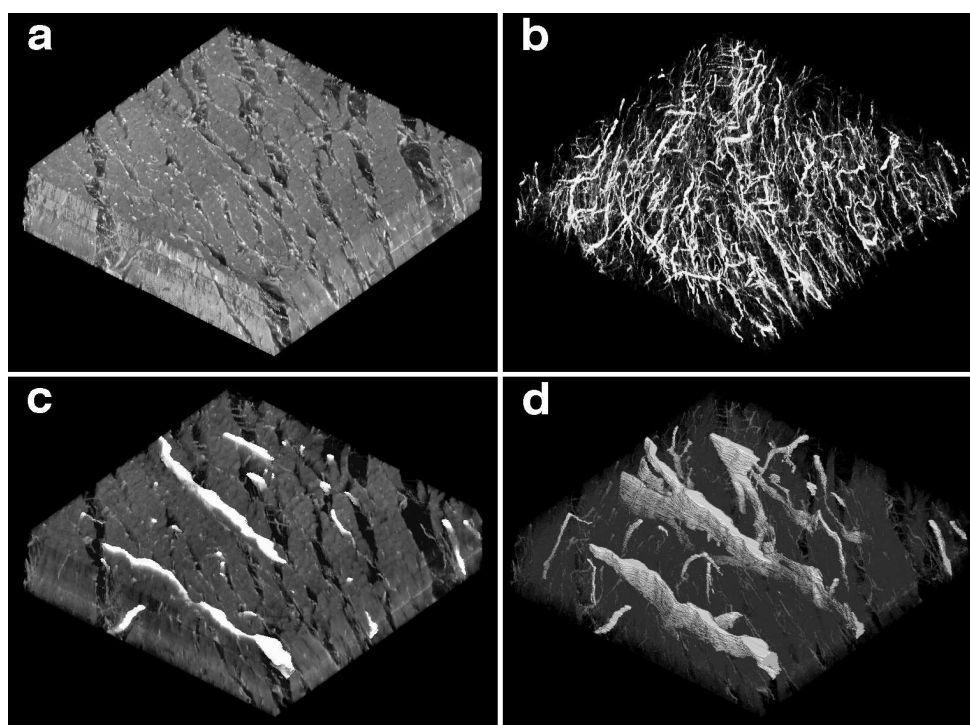


**Figure 3.** Reconstructed subvolumes ( $800 \times 800 \times 100 \mu\text{m}$ ). In the upper panel collagen is segmented and rendered (a) with and (b) without background due to myocytes. In the lower panel venous sinuses are segmented and rendered, (c) with, and, (d), without background. (From 1, with permission from the Royal Microscopical Society).

#### Development of automated techniques for acquiring extended volume images

Unfortunately, acquisition of an image volume such as that presented in Figure 1 requires weeks of painstaking work and this precludes the use of the manual approach outlined above for systematic morphometric analysis. For this reason, we are now developing an automated system that provides for computer controlled confocal imaging and milling of embedded tissue samples over extended volumes. The system consists of (i) a confocal microscope (Leica TCS 4D) with a Kr/Ar laser (Omnichrome) (ii) a variable speed Ultramill (Leica) which cuts to  $1\mu\text{m}$  over a 75mm path using diamond or tungsten carbide tips, and (iii) a three-axis translation stage (Aerotech) with xyz movement of 1000, 200 and 75mm, respectively at 100nm step size. The stage controls the positioning of specimens for imaging and milling (See Figure 4). Microscope and mill are supported above the translation stage using rigid mounting systems designed to facilitate alignment of imaging and cutting planes. The system is mounted on an anti-vibration table (Newport). Z-stack volume images are acquired for overlapping x-y areas that cover the region of interest. The imaged volume is then milled off and the process is repeated. A major advantage of this method is that alignment of the sample elements is maintained throughout the imaging and milling operations, thereby preserving spatial registration and making reconstruction of the complete volume image easier and faster.

The system is controlled using a dedicated computer

(Dell P4, 1.8GHz, 1GB RAM, Windows 2000) using custom software written using the LabVIEW™ programming language. A single user interface has been developed that enables image acquisition and milling to be controlled interactively or automatically and allows the operator to process, reconstruct and visualize the image volumes. The flexible user interface provides the ability to image chosen sub-volumes at high resolution, but placing them within the context of a large volume imaged at lower resolution.

Preliminary studies carried out with cardiac tissue specimens demonstrate that the system has the capacity to acquire 62.5 million voxels per hour, each averaged over 8 scans. This means that a fully-registered  $1\text{mm}^3$  image volume can be acquired at  $1\mu\text{m}$  resolution ( $10^9$  voxels) with 8× averaging, in 16 hours. This is a more than ten fold improvement with respect to our initial manual approach and further more modest improvement is seen to be possible with optimization of scanning and signal acquisition protocols.

The imaging rig is currently being used in a series of different projects including a longitudinal study of cardiac remodelling in spontaneously hypertensive rats throughout the course of their progress to heart failure and an analysis of the 3D organization of renal tubules and blood vessels in nephron segments. Particular emphasis is being given to extending the range of embedding and staining techniques that can be used with this automated volume imaging system.

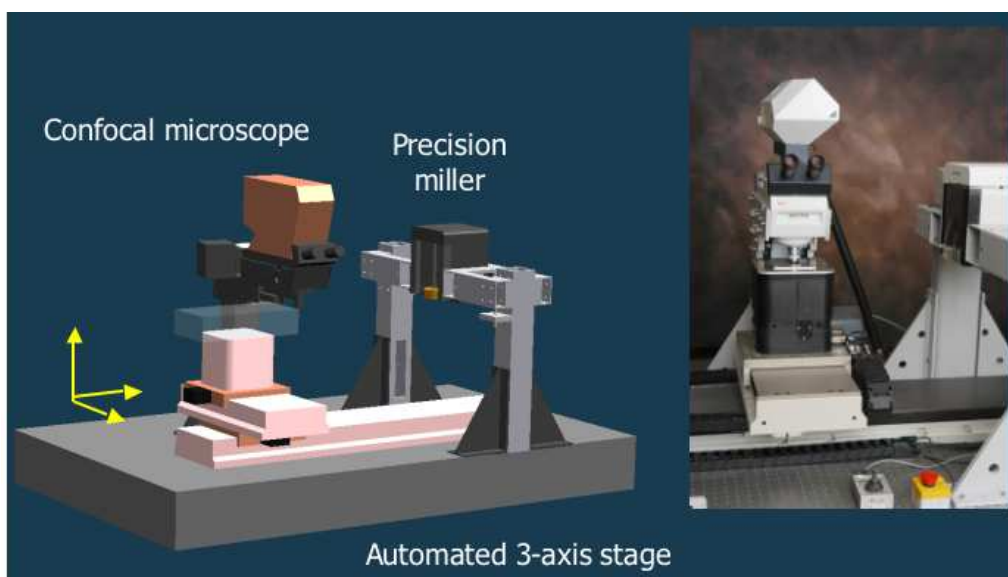


**Figure 4.** *The automated confocal imaging rig. The schematic indicates the arrangement of the confocal microscope, the ultramill and the three-axis translation stage. The inset photograph shows all three components and the anti-vibration table on which they are mounted.*

**Acknowledgments:**

Development of this imaging system was made possible by a grant from the Wellcome Trust.

**References:**

1. Young AA, LeGrice IJ, Young MA, Smaill BH. Extended confocal microscopy of myocardial laminae and collagen network. *J. Microsc.* 1998; **192**: 139-150.
2. Dolber PC, Spach MS. Conventional and confocal fluorescence microscopy of collagen fibres in the heart. *J. Histochem. Cytochem.* 1993; **41(3)**: 465-469.
3. Hooks DA, Tomlinson KA, Marsden SG, LeGrice IJ, Smaill BH, Pullan AJ, Hunter JP. Cardiac microstructure: implications for electrical propagation and defibrillation in the heart. *Circ. Res.* 2002; **91**: 331-338.

*Author for correspondence:*

Ian LeGrice  
Department of Physiology,  
University of Auckland,  
Auckland, New Zealand

Tel: +64 9 373 7599 ext 86206  
Fax: +64 9 373 7599  
Email: i.legrice@auckland.ac.nz

Received 27 July 2004, in revised form 17 August 2004.

Accepted ?? August 2004.

©I. LeGrice 2004.